MAS NMR Investigation of Molecular Order in an Ionic Liquid Crystal

*Sarah K. Mann,[a] Mohit K. Devgan,[b] W. Trent Franks,[a,c] Steven Huband,[a] Chi Long Chan,[b] Jeraime Griffith,[b] David Pugh,[†b] Nicholas J. Brooks,[b] Tom Welton,[b] Tran N. Pham,[d] Lisa L. McQueen,[e] Józef R. Lewandowski,[*c] and Steven P. Brown[*a]*

[a]Department of Physics, University of Warwick, Coventry CV4 7AL, U.K

[b]Department of Chemistry, Imperial College London, London, SW7 2AZ, U.K

[c]Department of Chemistry, University of Warwick, Coventry CV4 7AL, U.K

[d]GSK R&D, Stevenage, Hertfordshire SG1 2NY, U.K

[e]GSK R&D, Collegeville, PA 19426, U.S.A

ABSTRACT The structure and molecular order in the thermotropic ionic liquid crystal (ILC), [choline]$^{+}$[geranate(H)octanoate]$^{-}$, an analogue of Choline And GEranate (CAGE) which has potential for use as a broad-spectrum antimicrobial and transdermal and oral delivery agent, were investigated using magic-angle spinning (MAS) nuclear magnetic resonance (NMR), polarizing optical microscopy, small angle X-ray scattering (SAXS) and mass spectrometry. Mass spectrometry and the ^{1}H NMR chemical shift reveal that CAGE-oct is a dynamic system, with

metathesis (the exchange of interacting ions) and hydrogen exchange occurring between hydrogen-bonded/ionic complexes such as [(choline)(geranate)(H)(octanoate)], [(choline)(octanoate)$_2$(H)] and [(choline)(geranate)$_2$(H)]. These clusters, which are shown by mass spectrometry to be significantly more stable than expected for typical electrostatic ion clusters, involve hydrogen bonding between the carboxylic acid, carboxylate and hydroxyl groups, with rapid hydrogen bond breaking and reformation observed to average the ^{1}H chemical shifts. The formation of a partial bilayer liquid crystal (LC) phase was identified by SAXS and polarizing optical microscopy at temperatures below ~293 K. The occurrence of this transition close to room temperature could be utilized as a potential temperature-induced 'switch' of the anisotropic properties for particular applications. The presence of an isotropic component of approximately 23% was observed to coexist with the LC phase, as detected by polarizing optical microscopy and quantified by both ^{1}H–^{13}C dipolar-chemical shift correlation (DIPSHIFT) and ^{1}H double-quantum (DQ) experiments. At temperatures above the LC-to-isotropic transition, intermediate-range order (clustering of polar and non-polar domains), a feature of many ILs, persists. Site-specific order parameters for the LC phase of CAGE-oct were obtained from the measurement of the partially averaged ^{13}C–^{1}H dipolar couplings (D_{CH}) by cross-polarization (CP) build-up curves and DIPSHIFT experiments, and ^{1}H–^{1}H dipolar couplings (D_{HH}) by double quantum (DQ) build-up curves. The corresponding order parameters, S_{CH} and S_{HH}, are in the range 0 to 0.2, and are lower compared to those for smectic (*i.e.*, layered) phases of conventional non-ionic liquid crystals, resembling those of lamellar phases formed by lyotropic surfactant-solvent systems.

1. Introduction

As the name suggests, the liquid crystalline state of matter is an intermediate between liquids and solids; there is long range order but the molecules themselves are mobile. Liquid Crystals (LCs) can form under suitable temperature (thermotropic LCs) or concentration (lyotropic LCs) conditions. A subset of LCs, ionic LCs (ILCs) carry charges, and thus combine the characteristics of LCs and ionic liquids[1-2] (ILs). ILCs combine the conductivity, low vapor pressure, and tuneability (the ability to select or modify properties by the appropriate choice of the anion and cation) of ILs, with the anisotropic properties of LCs. This unique combination of properties has generated interest in ILCs,[3-5] which may be used in a broad range of fields, with applications including LC displays,[6] as electrolytes in dye-sensitized solar cells,[7-9] as ordered reaction media or templates in synthetic chemistry,[10-12] and for biological applications.[13-14] The majority of ILCs are based on typical organic nitrogen cations (*e.g.*, imidazolium, ammonium and pyridinium) substituted with one or more long alkyl chain and inorganic anions (*e.g.*, halides, $[BF_4]^-$, $[PF_6]^-$), and form smectic (*i.e.*, layered) phases, exhibiting partial positional order, in addition to orientational order.[3] They typically display considerably less orientational order compared to non-ionic thermotropic LCs, instead resembling the lyotropic lamellar phases of surfactant-water systems.[15-16] Advancing our understanding of ILC structure and dynamics at an atomic level will enable and promote the development of novel ILCs as well as further applications for ILCs.

Choline And GEranate (CAGE) is a broad-spectrum antimicrobial and a transdermal and oral delivery agent.[17-22] The most effective formulation of CAGE is composed of choline, geranic acid and the geranate anion in a 1:1:1 ratio ($[choline]^+[geranate_2(H)]^-$),[21] which has been described as both an IL, and a deep eutectic solvent (DES),[20, 23] a eutectic mixture of two or more components (in some cases both neutral and ionic species) that typically interact via strong hydrogen bonding. We have modified CAGE, replacing one equivalent of geranic acid with octanoic acid, to form a novel stable thermotropic ILC, CAGE-octanoic acid (CAGE-oct; Figure 1). The LC-to-isotropic

phase transition of CAGE-oct occurs close to room temperature (~293 K), which may be exploited as a temperature-induced 'switch' of the anisotropic properties for specific applications.

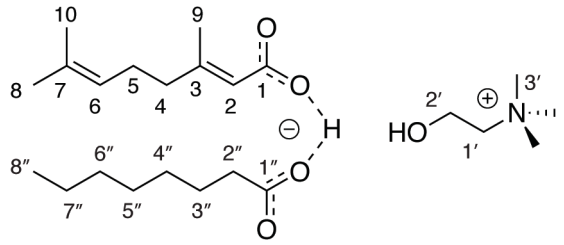

Figure 1. Primary structure of CAGE-oct. The numbering shown is used for NMR assignments throughout the text.

When considering structure and order in such materials, both the time-scale and length-scale are of importance. In contrast to a so-called 'isotropic' liquid (where there can still be some short-range ordering), LCs exhibit long-range positional and/or orientational order; the molecular positions and relative orientations are correlated over longer distances. Aspects of the structure (*e.g.*, shape of the constituent molecules and nano-scale segregation of molecular components into distinct regions) determine the formation of LC phases. The segregation of incompatible parts of the molecules (*e.g.*, non-polar aliphatic chains from polar regions), as well as attractive forces (*e.g.*, ionic interactions or hydrogen bonding) drive the formation of long-range positional order in ILCs.

Small-angle X-ray scattering (SAXS) and nuclear magnetic resonance (NMR) spectroscopy are complementary techniques to investigate LCs.[24] While SAXS identifies long-range order, NMR yields local atomic-level structure, *e.g.*, about specific intermolecular hydrogen bonding interactions, and is sensitive to molecule/segment/bond orientations. Specifically, the dipolar couplings between spins report on order: the dipolar coupling depends on the timescale and amplitude of molecular motion, because motion averages the couplings. Compared to an isotropic

liquid where the molecules undergo rapid tumbling and all orientations are sampled, such that the dipolar couplings are averaged to zero, in anisotropic LC phases there is a preferential orientation and the dipolar coupling is not completely averaged out. The ratio of the partially averaged residual dipolar coupling (RDC, D_{res}), to its unaveraged value (*i.e.* the value in the rigid limit, D_{rigid}) provides the order parameter, $S = D_{res}/D_{rigid}$. S ranges from 0 for isotropic systems, to 1 for completely rigid systems (see Section S1 for further details on the dipolar coupling and order parameter).

In solid-state NMR, magic-angle spinning (MAS) averages anisotropic interactions so that high-resolution spectra can be obtained. Radiofrequency (rf) pulses can be applied that interfere with the MAS averaging, and thus recouple the interactions, and the strength of the interaction can be measured. One such approach is the much-employed solid-state NMR approach of ^{1}H–^{13}C cross-polarization (CP), whereby long rf pulses are applied simultaneously with the same nutation frequency (under MAS, this so-called Hartmann-Hahn matching condition is adjusted by a small integer multiple of the spinning frequency) to both the ^{1}H and ^{13}C nuclear spins: ^{13}C–^{1}H heteronuclear dipolar couplings may be obtained from ^{1}H–^{13}C CP build-up curves. If there is a dominant dipolar interaction, the polarization transfer shows oscillatory behavior where the frequency of oscillations is directly proportional to the dipolar coupling constant.[25] CP build-up curves or variants such as Lee-Goldburg (LG) CP have been used to obtain RDCs and the related S_{CH} order parameters in various dynamic systems, including polymers,[26] and LCs.[27-28]

A complement to probing ^{13}C–^{1}H dipolar coupling is the measurement of ^{1}H-^{1}H homonuclear dipolar couplings, and the related order parameter S_{HH}.[29-35] ^{1}H-^{1}H RDCs can be quantified by ^{1}H double quantum (DQ) MAS spectroscopy,[36-40] from which the value of the dipolar coupling constant can be extracted either by fitting the intensity of the build-up behavior with varying DQ excitation time (τ_{DQ}) or by analyzing the spinning sideband pattern in a 2D spectrum recorded with

fixed τ_{DQ}. Brown *et al.* utilized ^{1}H-^{1}H residual dipolar couplings to study rotation of the aromatic core in columnar hexabenzocoronene LCs, as well as differential mobility along the alkyl chains in a triphenylene-based mesogen.[29-30] ^{1}H-^{1}H RDCs have also been used to investigate chain dynamics in polymer systems,[31, 41-43] and for the study of lipid membranes with guest molecules.[44]

Despite the interest in ILCs, and the potential of NMR for probing structure and order, very few NMR studies have been reported on ILC materials. Recently, Di Pietro *et al*.[45] and Dai *et al.*[15, 46] reported static NMR studies of ILCs containing imidazolium cations, and inorganic anions ($[NO_3]^-$, Cl^- and $[BF_4]^-$). The MAS NMR techniques used in this paper have not, to our knowledge, thus far been used to investigate ILCs.

In this work, we investigate the short-range (interactions between ions) and long-range structure (the occurrence of the partial bilayer LC phase), and molecular order of CAGE-oct, by MAS NMR, SAXS, and mass spectrometry. Mass spectrometry and the ^{1}H NMR chemical shift provide a 'snapshot' of the hydrogen-bonding structures/ionic complexes present in CAGE-oct. SAXS reveals the intermediate-range order of CAGE-oct above the LC-to-isotropic transition, and long-range order of the partial bilayer LC phase at temperatures below ~293 K. The LC texture and LC-to-isotropic phase transition was also viewed via polarizing optical microscopy. Residual ^{13}C–^{1}H and ^{1}H-^{1}H dipolar couplings are measured by means of ^{1}H–^{13}C CP and ^{1}H double-quantum (DQ) build-up curves, so as to obtain order parameters, S_{CH} and S_{HH}, which quantitatively describe the amplitude of motion of the ions (and molecular segments/bonds) that comprise CAGE-oct.

2. Experimental

2.1 Sample preparation: Choline bicarbonate (80 wt.% solution in water) and octanoic acid were purchased from Sigma and used as received. Geranic acid (85%) was purchased from Sigma but was recrystallized five times from cold HPLC-grade acetone (VWR) before use. A solution of

choline bicarbonate (2.67 g, 12.96 mmol) in water (3 mL) was added slowly to a stirred solution of geranic acid (2.18 g, 12.96 mmol) in ethanol (8 mL). The mixture was stirred for 2 hours, then 1-octanoic acid (1.87 g, 12.96 mmol) was added dropwise. After 16 hours, volatiles were removed in vacuo yielding a colorless oil. This was azeotropically dried using toluene (2 × 15 mL) then dried under high vacuum at 45 °C for 16 hours. The resulting colorless oil solidified into an opaque, white wax on standing (yield: 4.81 g, 89%). Further details, including all spectroscopic data, can be found in the SI (Section S2 and Figures S1-S4).

2.2 Polarizing Optical Microscopy: Samples were placed into flat glass capillary tubes and supported on a glass slide for imaging using a Nikon Eclipse E600POL microscope with Nikon CFI Achromat 4X,10X and 20x objective lenses. Images were acquired using a QICAM Fast 1394 CCD camera (QImaging). Temperature control was achieved using a Linkam LTS 350 temperature-controlled microscope stage with a Linkam TMS 94 temperature controller (Linkam Scientific Instruments), coupled with a liquid nitrogen pump for cooling. Image analysis was carried out using the open source software package ImageJ.[47]

2.3 Mass spectrometry: Mass spectra were obtained by gently warming CAGE-oct until it melted then directly injecting it into a Waters single quadrupole detector at 4.2 kV capillary voltage using electrospray ionization (both positive and negative modes were obtained).

2.4 SAXS: SAXS measurements were made using a Xenocs Xeuss 2.0 equipped with a micro-focus Cu Kα source collimated with Scatterless slits. The scattering was measured using a Pilatus 300k detector with a pixel size of 0.172 mm × 0.172 mm. The distance between the detector and the sample was calibrated using silver behenate ($AgC_{22}H_{43}O_2$), giving a value of 0.540(5) m. The

magnitude of the scattering vector (q) is given by $q=4\pi \sin(\theta)/\lambda$, where 2θ is the angle between the incident and scattered X-rays and λ is the wavelength of the incident X-rays. This gave a q range for the detector between 0.023 $Å^{-1}$ and 0.73 $Å^{-1}$ in the horizontal plane. The 2D detection image was integrated as a function of q producing the 1D intensity versus q data. For measurements as a function of temperature, the samples were held between two Kapton windows in a Linkam HFSX 350 furnace. Separate measurements of the Kapton windows and furnace were used for background corrections.

2.5 MAS NMR: MAS NMR experiments were performed on a Bruker Avance III spectrometer operating at a ^{1}H Larmor frequency of ν_{0H} = 500 MHz (11.7 T), using a 3.2 mm double-resonance MAS probe. A spinning frequency, ν_R, of 5 kHz was used. The temperature was calibrated using methanol, as described in the Bruker Instruments manual, with all stated temperatures being corrected by this procedure. The ^{1}H and ^{13}C 90° pulses were of duration 2.5 μs and 5 μs, respectively (corresponding to nutation frequencies, $\nu_{1,H}$ = 100 kHz, and $\nu_{1,C}$ = 50 kHz).

For ^{1}H–^{13}C CP experiments, the ^{1}H and ^{13}C nutation frequencies were approximately 52.5 and 47.5 kHz, respectively. For the 2D heteronuclear correlation (HETCOR) experiment, CP was achieved using a 70 to 100% ramp[48] on the ^{13}C channel, whereas CP build-up curves were recorded without a ramp to allow for quantitative determination of the dipolar coupling, D_{CH}. SPINAL-64[50] heteronuclear decoupling was applied during acquisition at a ^{1}H nutation frequency of 52.5 kHz, corresponding to a pulse duration of 9.0 μs. Additional parameters are provided in Section S3.1.

DIPSHIFT curves were recording using both CP and direct polarization (DP) for the initial excitation procedure. For the ^{1}H–^{13}C CP DIPSHIFT experiment, the ^{1}H and ^{13}C nutation frequencies were 52.5 and 47.5 kHz, respectively. CP was achieved using a 70 to 100% ramp[48] on the ^{13}C channel for a contact time of 5 ms. Eight rotor periods of recoupling (N = 8) were used.

The decoupling schemes for homonuclear and heteronuclear decoupling were frequency-switched Lee-Goldburg (FSLG)[51-52] and SPINAL-64,[50] respectively, applied at a nutation frequency of 62.5 kHz. Additional parameters are provided in Section S3.1.

For ^{1}H DQ experiments, the excitation and reconversion of ^{1}H DQ coherences was achieved using the POST-C7 recoupling method[53] at a ^{1}H nutation frequency of 35 kHz. For ^{1}H DQ build-up curves (see pulse sequence in Section 3.7 below), DQ selection (more accurately for $4n + 2$ coherence orders, although the DQ coherence order can be assumed to be dominant) was performed using a four-step phase cycle for the reconversion block (0°, 90 °, 180 °, 270 °) while inverting the receiver phase for alternating transients (0°, 180 °, 0 °, 180 °), so as to select $\Delta p = \pm 2$, where p is the coherence order. A reference experiment was recorded in the same manner, however keeping the receiver phase constant. Additional parameters are provided in Section S3.1.

^{1}H and ^{13}C chemical shifts are referenced to tetramethylsilane (TMS) at 0 ppm using L-alanine as a secondary reference (1.1 ppm for the lower ppm ^{1}H resonance and 177.8 ppm for the higher ppm ^{13}C resonance), corresponding to adamantane at 1.85 ppm (^{1}H)[54] and 38.5 ppm (^{13}C).[55]

2.6 Simulations and fitting: CP build-up and CP T_2-recDIPSHIFT curves were fit using a simplex minimization implemented in the opt1.0 package in SIMPSON (v4.2.1).[56-57] Further details of the simulations and error analysis and representative SIMPSON input files are provided in the SI.

3. Results and Discussion

3.1 Small Angle X-ray Scattering

SAXS patterns for CAGE-oct at temperatures ranging from 263 to 313 K are shown in Figure 2a. The first order scattering peak provides information on the ordering, since the layer distance by Bragg's Law is $d = 2\pi/q_{max}$. A single peak is observed at q ≈ 0.29 Å^{-1} (at 273 K), corresponding

to a repeat distance of 22 Å. The first order scattering peak shifts to higher q values at higher temperatures, corresponding to a decrease in the repeat distance, and indicating a negative thermal expansion upon heating (Figure S6). At temperatures below ~293 K, the first-order scattering peak is narrow and intense, indicative of a liquid-crystalline phase. The repeat distance of 22 Å (at 273 K), roughly the length of two molecules of octanoic/geranic acid, is analogous to the spacing observed in bilayer membrane systems. Smectic LC phases (or lamellar phases) are the most commonly observed phase for ILCs and are characterized by the stacking of layers that exhibit some positional and orientational order (Figure 2b). The layer formation of smectic ILCs is driven by Coulombic forces and nano-segregation of the charged moieties from the hydrophobic chains:[5] forces that are expected to dominate the intermolecular interactions of CAGE-oct. In contrast, the nematic phase, which displays only orientational order, is rarely observed for ILC systems[61-62] and is unlikely to occur for CAGE-oct owing to the lack of nematic phase favoring features such as π-π interactions (*i.e.* aromatic rings).[63]

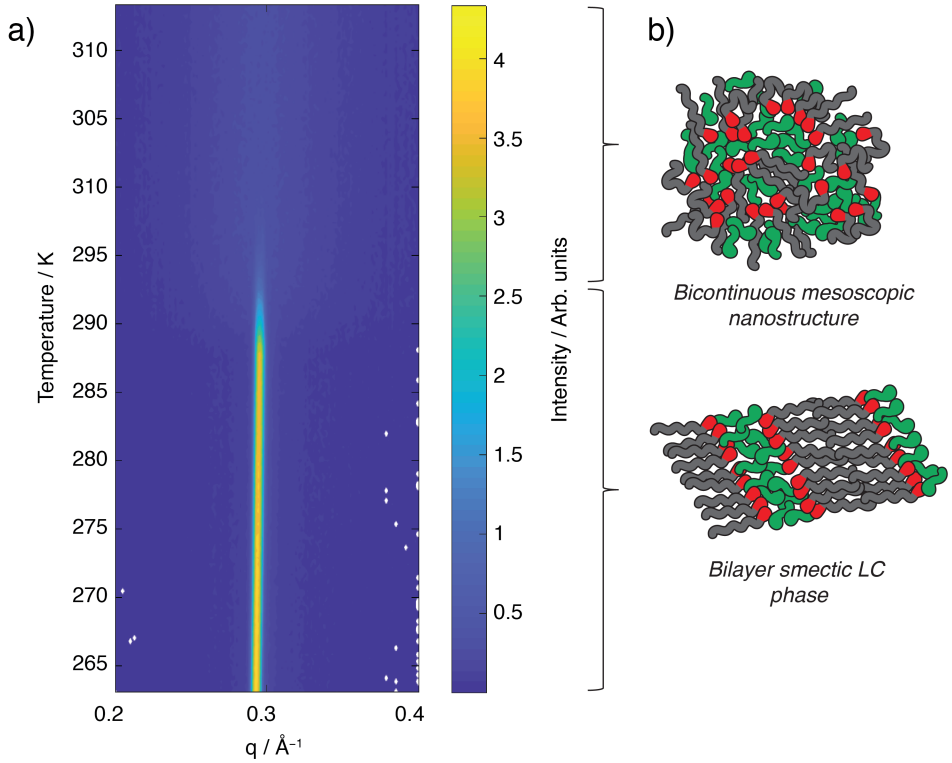

Figure 2. (a) SAXS contour plot showing the temperature behavior of the first order scattering peak for CAGE-oct. (b) Schematic illustration of a bicontinuous mesoscopic nanostructure and a bilayer smectic LC phase.

At temperatures above ~293 K, the SAXS profile becomes significantly broader, and closely resembles those observed in ILs based on the 1-alkyl-3-methylimidazolium cation ($[C_nC_1im]^+$) of various intermediate alkyl chain lengths ($3 < n < 10$).[64-65] Whilst a micelle-like model for self-assembly in ILs (with alkyl chains longer than a butyl group) was initially suggested to account for the diffraction peak at low-q,[65-66] more recent studies have shown that the diffraction profile may be interpreted as a bicontinuous sponge-like mesoscopic structure,[67-69] resulting from clustering of polar and non-polar domains (Figure 2b). This has further been evidenced by simulations for a number of ILs.[70-71] We note that even the commonly referred to 'isotropic state'

of many ILs displays some degree of nanoscale structure and charge ordering, although not to the same extent or length scale as for ILCs. The persistence of some short-range order above the smectic-to-isotropic transition temperature has been observed in carbohydrate-based LCs, where a low enthalpy/entropy Sm-to-isotropic transition was suggested to be a result of hydrogen-bonded aggregates remaining in the isotropic liquid phase.[72-73]

3.2 Polarizing Optical Microscopy

Figure 3 shows a polarizing optical microscopy image of the LC phase of CAGE-oct at 278 K. There appear to be two distinct birefringent areas with larger scale and smaller scale patterning (solid red oval and dashed red oval, respectively). Both of these optical textures are conic fan textures characteristic of a smectic A (SmA) structure[74-78] and the apparently distinct patterns are likely to arise from differences in nucleation.[79] In addition, there are regions with no birefringence present between LC domains, indicating isotropic liquid regions. These results are consistent with the presence of an isotropic component coexisting with the LC phase as detected by NMR (discussed below in Section 3.7 and in Section S4.2). On heating, the LC phase melts to an isotropic phase between 290 and 298 K (Figure S7); this transition is also seen in the SAXS results described above. On cooling from the isotropic phase, the first birefringence patterns appear between 291 and 293 K.

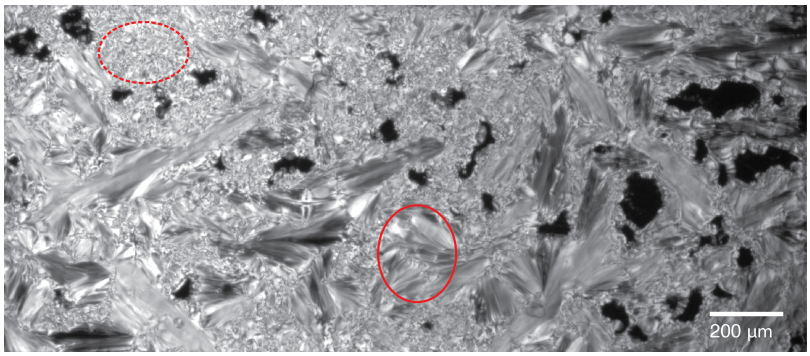

Figure 3. Polarizing optical micrograph (× 4) of CAGE-oct, showing the LC texture at 278 K. The red ovals highlight the two distinct birefringent patterns.

3.3 Mass Spectrometry

Careful study of the negative ion mass spectrum of CAGE-oct (see Section S2 and Figures S3 and S4 for the full spectrum analysis) reveals evidence of interactions between choline and carboxylate anions. As expected, both 'free' octanoate and geranate anions are observed under mass spectrometry conditions, but an ion corresponding to CAGE-oct, $[(\text{choline})(\text{octanoate})(\text{geranate})]^-$, is also seen at a mass to charge ratio (m/z) 414 (with loss of a proton). This peak is about 70% of the intensity of 'free' octanoate peak, implying that these clusters are significantly more stable than would otherwise be expected from simple electrostatic-based ion clustering, probably due to the hydrogen bonding interactions between the hydroxyl group of choline cation and the carboxylate anions. Further peaks at m/z 390.4 and 438.4 correspond to $[(\text{choline})(\text{octanoate})_2]^-$ and $[(\text{choline})(\text{geranate})_2]^-$, respectively. The ratio of these three clusters is close to the statistically expected 1:2:1 even though CAGE-oct was synthesized by adding one molar equivalent of 1-octanoic acid to *in situ*-generated choline geranate, implying anion metathesis is taking place. These peaks are significantly more intense (at least an order of magnitude) than those of the $[(\text{anion})_2(\text{H})]^-$ species, suggesting that there is a strong association of the choline cation with the carboxylate anions. Many larger ion clusters generated by electrostatic

ion clustering, for example m/z 661.6 $[(choline)_2(octanoate)_2(geranate)]^-$, were observed at <5% of the intensity of 'free' octanoate which is more typical of electrostatic ion clusters, especially those found in the mass spectra of ionic liquids.[80]

3.4 ^{1}H Variable Temperature MAS NMR

In order to investigate the nature of the interactions between the components of neat CAGE-oct, proposed by mass spectrometry, we performed 1D ^{1}H MAS NMR spectroscopy (Figure 4a). A single set of ^{1}H resonances is observed for each of the choline, geranate and octanoate components, consistent with rapid anion metathesis taking place, which would result in averaging of the chemical shifts between clusters such as [(choline)(geranate)(H)(octanoate)], $[(choline)(octanoate)_2(H)]$ and $[(choline)(geranate)_2(H)]$ which have been observed by mass spectrometry (see Section 3.3). The mechanism of this metathesis is key to establishing whether CAGE-oct (and, by extension, CAGE) can be classified as an ionic liquid or not. If the mechanism generates free octanoic acid (or geranic acid) then, by definition, the mixture is no longer 'a liquid composed entirely of ions' and it cannot be considered as an ionic liquid. However, if the mechanism does not require the formation of free acid to proceed, then CAGE-oct can be considered to meet the definition of an ionic liquid. Thus far, we have been unable to find any experimental evidence for the existence of free acid in CAGE-oct, either by mass spectrometry or ^{1}H MAS NMR, implying that it does fit the definition of an ionic liquid.

A single peak is observed for the COOH and OH ^{1}H resonances, which is indicative of fast chemical exchange on the NMR timescale between the carboxylic acid proton and the hydroxyl proton of choline. The presence of hydrogen bonding between the components is evidenced by the COOH/OH ^{1}H resonance appearing at 9.5 ppm (at 273 K), a value that corresponds to the average of the COOH and OH resonances, which are expected to lie at approximately 13-15 and 5-6 ppm,

respectively. Note that the exact position of this peak is highly sensitive to ppm concentrations of water in the sample. The chemical shift of protons participating in hydrogen bonds is known to be temperature sensitive due to changes in the degree of excitation of the hydrogen-bond-stretching vibrational mode,[81-84] and has been shown to correlate with the nature and strength of the hydrogen bond.[84-87] The chemical shift temperature coefficient, $TC = \Delta\delta(^1H)/\Delta T$, determined in the range 268 to 323 K, of $-[6.2 \pm 0.1] \times 10^{-3}$ ppm K^{-1} (Figure 4b), is consistent with intermolecular hydrogen bonding.[88-89] The hydrogen bonding arrangement involves the carboxylic acid, carboxylate and hydroxyl groups, possibly as hydrogen-bonded clusters such as [(choline)(geranate)(H)(octanoate)], as suggested by mass spectrometry, and is likely dynamic, where rapid formation and subsequent breaking of hydrogen bonds occurs between the carboxylic acid, carboxylate, and hydroxyl groups. The reported hydrogen bond lifetimes for ILs are typically on the order of picoseconds.[90-92] The presence of hydrogen bonding has, in some cases, been reported to drive the formation of LC phases.[93]

No discontinuity in the temperature-dependent chemical shift of the COOH/OH resonance was observed at the LC-isotropic phase transition temperature of CAGE-oct (as identified from the SAXS data in Figure 2a). The same temperature coefficient for the LC and isotropic phase of CAGE-oct suggests that a similar hydrogen bonding arrangement persists in the isotropic phase, consistent with reports of the behavior of other LC systems.[72-73]

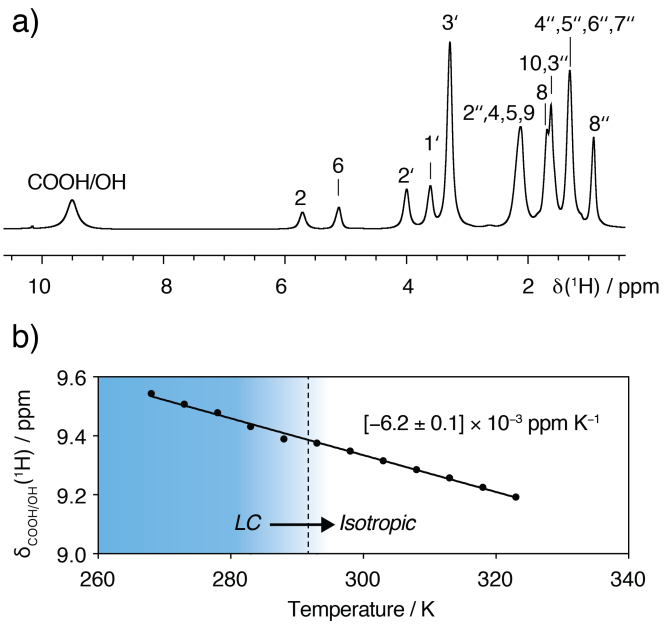

Figure 4. (a) A ^{1}H 1D one-pulse MAS NMR spectrum (ν_{0H} = 500 MHz, ν_r = 5 kHz) of CAGE-oct recorded at 273 K. (b) The temperature dependence of the COOH/OH resonances, with best fit line to determine the temperature coefficient, TC. The dashed line indicates the LC to isotropic transition as observed by SAXS.

3.5 2D ^{1}H–^{13}C CP Heteronuclear Correlation MAS NMR

A 2D ^{1}H–^{13}C CP-HETCOR MAS spectrum of CAGE-oct is shown in Figure 5. The spectrum was recorded at 273 K, as were all further NMR experiments reported in this study; this temperature is below the LC-to-isotropic transition temperature indicated by SAXS and polarizing microscopy. Under 5 kHz MAS, all of the ^{13}C resonances are resolved. Using a relatively long contact time of 2.5 ms, only a single ^{1}H–^{13}C cross peak was observed for all carbons with a directly bound proton corresponding to the one-bond C–H connectivities. This indicates that the dipolar couplings are highly averaged by molecular motion, implying that CAGE-oct is a dynamic system which is undergoing a rapid anion metathesis on the NMR timescale. For comparison, in rigid

solids, cross peaks corresponding to longer-range C–H proximities can already be observed at contact times of only 200 μs.[94]

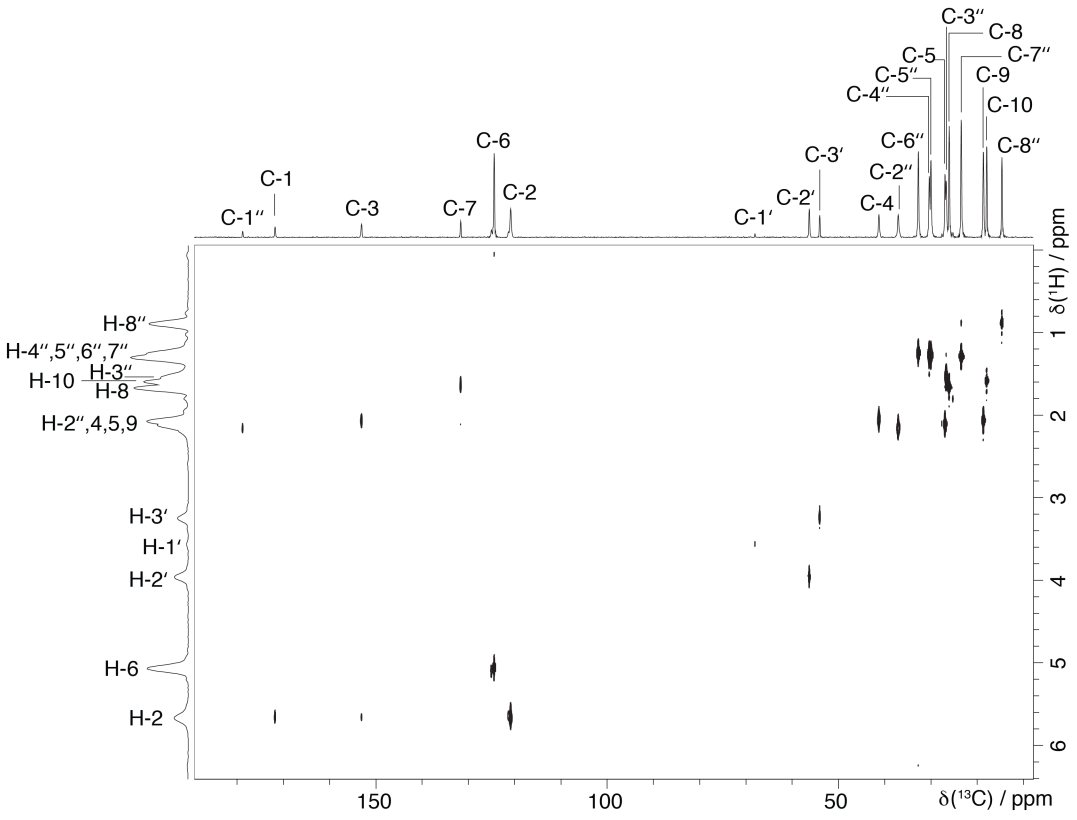

Figure 5. A $^{1}H–^{13}C$ HETCOR MAS NMR spectrum (ν_{0H} = 500 MHz, ν_r = 5 kHz) with skyline projections of CAGE-oct, recorded with a CP contact time of 2.5 ms at 273 K. The base contour level is at 3.9% of the maximum peak intensity.

We note the absence of any contacts to the COOH/OH proton (see Figure S8 for the full spectral range) despite the carbonyl carbons (C-1 and C-1′′) showing a dipolar coupling to the protons of their adjacent carbon (H-2 and H-2′′, respectively), which are expected to be located slightly further away than the acidic proton. This suggests that the absence of CP from the COOH/OH proton is due to motion of the exchangeable proton between the ions; *i.e.*, the COOH and OH

protons do not stay within close enough proximity of any one carbon for long enough for the observable build-up of $^{1}H–^{13}C$ CP signal to occur.

3.6 $^{1}H–^{13}C$ MAS NMR: C–H Dipolar Couplings

In order to investigate the molecular dynamics of CAGE-oct in the LC phase, CP build-up curves were recorded to quantify the C–H dipolar couplings. The magnitude of the ^{13}C-^{1}H dipolar coupling is dependent on both the distance and orientation of the involved nuclei. For specific chemical moiety, e.g., a covalently bound C–H, there is a fixed internuclear distance such that the measured dipolar couplings therefore report on the extent of averaging of the dipolar coupling by motions that are fast on the timescale of the NMR experiment (> 100 kHz). CP build-up curves were recorded by incrementing the CP contact time up to a maximum of 2 ms (Figure 6). Clear oscillatory behavior was observed for all of the CH and CH_2 groups of the geranate and octanoate with a maximum intensity occurring between 100-600 μs, whilst smoother curves with slower initial build-up and faster relaxation were observed for the methyl groups. Dipolar couplings for all carbons to their directly bonded protons were obtained by iterative least squares fitting to simulated build-up curves (using SIMPSON,[56-57] see Sections 2.6 and S4.1) for a 2-, 3- and 4-spin system for CH, CH_2 and CH_3 groups respectively, excluding C-1′ and C-3′ of choline for which the CP intensity was too low to accurately obtain D_{res}. The inclusion of proton-proton dipolar couplings was found to have no significant effect on the fits (Table S1) and therefore only the CH dipolar coupling was included in the fitting (see Figure S9 and further discussion in Section S4.1). The inclusion of a single exponential relaxation time as a second fitting parameter also did not significantly alter the obtained value of D_{res} (Table S1), however a statistically significant improvement in the fit was obtained for some curves and the relaxation term was therefore

included. The resulting best-fit curves are shown by the solid lines in Figure 6 and the dipolar couplings, which ranged from 0.88 to 3.95 kHz are given in Table 1.

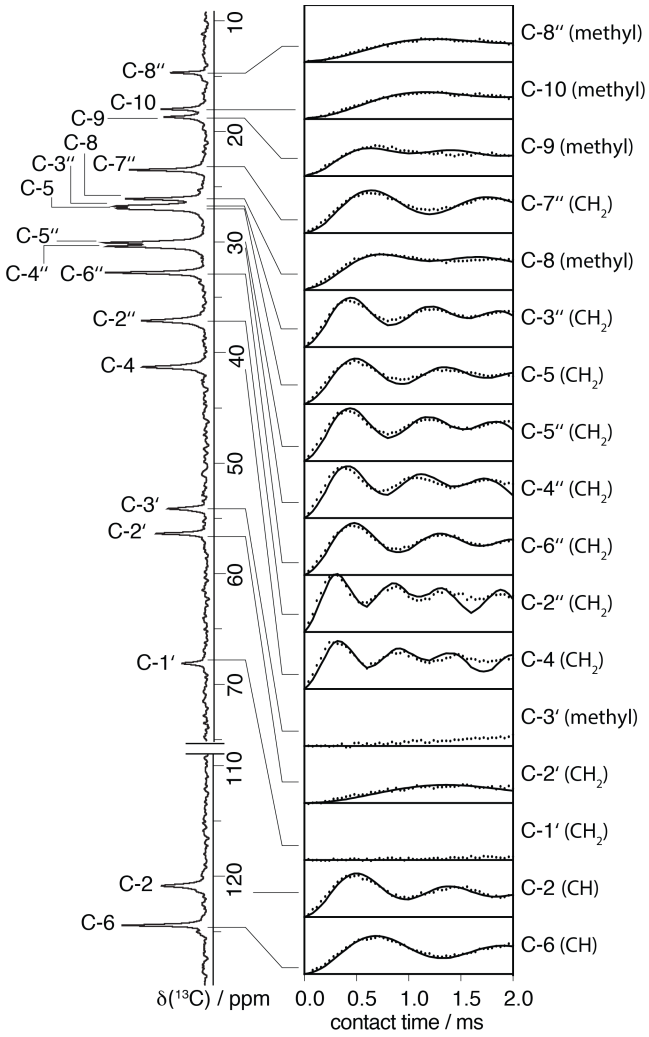

Figure 6. $^{1}H–^{13}C$ CP MAS NMR (ν_{0H} = 500 MHz, ν_r = 5 kHz) build-up curves for CAGE-oct recorded at 273 K. The best-fit simulations are depicted as solid lines for dipolar coupling constants, D_{CH}, reported in Table 1. The one-dimensional spectrum shown vertically was recorded with a CP contact time of 2.5 ms.

Table 1. Results of fits of the experimental $^{1}H–^{13}C$ CP build-up curves (see Figure 6, as recorded at 273 K) and CP-T_2-recDIPSHIFT profiles (see Figure S10b, as recorded at 273 K). Fitting details are given in Sections 2.6, 3.6 and S3.2.

		CP build-up		T_2-recDIPSHIFT	
Peak	Type	$D_{res}/2\pi$	S_{CH}	$D_{res}/2\pi$	S_{CH}
C-9	Methyl	1.71 ± 0.06	0.224 ± 0.008	1.12 ± 0.04	0.147 ± 0.005
C-8	Methyl	1.6 ± 0.1	0.21 ± 0.01	1.09 ± 0.03	0.143 ± 0.004
C-2″	CH_2	3.95 ± 0.07	0.174 ± 0.003	3.8 ± 0.2	0.17 ± 0.01
C-4	CH_2	3.67 ± 0.08	0.162 ± 0.004	3.6 ± 0.2	0.159 ± 0.008
C-2	CH	3.27 ± 0.06	0.145 ± 0.003	2.75 ± 0.06	0.122 ± 0.003
C-4″	CH_2	3.08 ± 0.06	0.136 ± 0.003	3.00 ± 0.08	0.132 ± 0.004
C-10	Methyl	0.97 ± 0.03	0.127 ± 0.004	0.78 ± 0.02	0.102 ± 0.003
C-5″	CH_2	2.83 ± 0.06	0.125 ± 0.002	2.86 ± 0.04	0.126 ± 0.002
C-3″	CH_2	2.75 ± 0.07	0.121 ± 0.003	2.76 ± 0.06	0.122 ± 0.003
C-8″	Methyl	0.92 ± 0.03	0.120 ± 0.003	0.73 ± 0.03	0.096 ± 0.004
C-6″	CH_2	2.53 ± 0.05	0.112 ± 0.002	2.57 ± 0.09	0.113 ± 0.004
C-5	CH_2	2.45 ± 0.07	0.108 ± 0.003	2.40 ± 0.06	0.106 ± 0.003
C-6	CH	2.41 ± 0.03	0.107 ± 0.002	2.24 ± 0.02	0.099 ± 0.001
C-7″	CH_2	1.86 ± 0.03	0.082 ± 0.001	1.90 ± 0.03	0.084 ± 0.001
C-2′	CH_2	0.88 ± 0.03	0.039 ± 0.001	0.88 ± 0.04	0.039 ± 0.001
C-1′	CH_2	–[a]	–[a]	–[a]	–[a]
C-3′	Methyl	–[a]	–[a]	–[a]	–[a]

[a]Too low to extract from the experimental data

In addition to the measurement of $^{1}H–^{13}C$ dipolar couplings by means of CP MAS NMR build-up curves, these were also determined by the dipolar-chemical shift correlation (DIPSHIFT) method. As the CH dipolar couplings in CAGE-oct are relatively weak, a recoupled version of the original DIPSHIFT experiment was utilized, where the phase accumulated due to the evolution under the dipolar coupling during t_1 is amplified by a REDOR-like train of π pulses .[95] We further chose a variant of the DIPSHIFT experiment reported by Cobo *et al*. where the evolution time under heteronuclear dipolar coupling is not constant (in contrast to frequently used constant time experiments), and a potential T_2 decay indicative of intermediate time-scale motions is possible.[43] The pulse sequence for the T_2-recDIPSHIFT experiment is shown in Figure S10a. After excitation (CP or DP), the magnetization evolves during a variable time t_1 under the influence of the heteronuclear dipolar interaction, whilst the ^{1}H homonuclear coupling is suppressed by FSLG decoupling. DIPSHIFT curves are shown in Figure S10b. The resulting DIPSHIFT profiles (Figure S10b) return to close to the initial maximum intensity at $t_1 = N\tau_r$, indicating that there are no significant intermediate time-scale motions with rates between 1 to 100 kHz in CAGE-oct.[96-97] This confirms that our treatment of the reduction in the dipolar coupling described by the order parameter as providing information on the amplitude of fast motions is valid. A discussion of the differences in DP- and CP-DIPSHIFT profiles is provided in Section S4.2. The values of D_{res} obtained from fits of the CP-DIPSHIFT profiles are given in Table 1 and the resulting order parameters, S_{CH}, are graphically compared to those obtained from CP build-up curves in Figure 7. Overall, the two methods produced values with very good agreement, within error for most of the sites. Notably, the largest discrepancies between the two methods were observed for the methyl groups (C-9, C-8, C-10 and C-8′′). The CP build-up curves of the methyl groups (Figure 6) did not show clear oscillations as were observed for the CH and CH_2, which could account for slightly less accurate values.

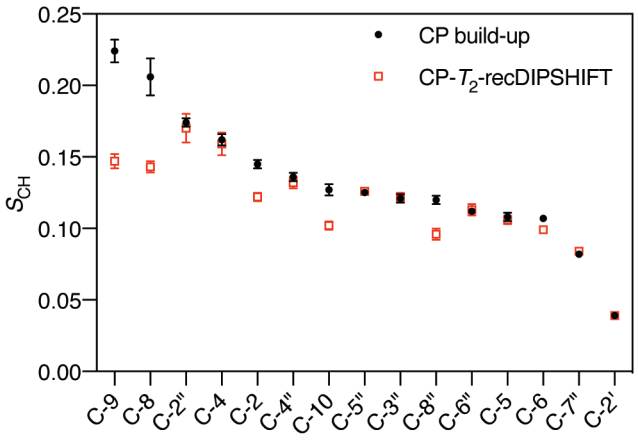

Figure 7. Comparison of S_{CH} obtained from CP build-up curves (Figure 6, Table 1) and CP-T_2-recDIPSHIFT experiments (Figure S10b, Table 1) at 273 K. The atom order corresponds to decreasing S_{CH} as determined from CP build-up curves.

3.7 ^{1}H DQ MAS NMR Build-up Curves: H–H Dipolar Couplings

As shown in the previous section, dipolar couplings can be obtained from ^{1}H–^{13}C CP MAS NMR build-up curves, however, this method has some disadvantages due to the low signal-to-noise ratio of carbon detection and inaccuracies in the determination of the smaller coupling constants below 1 kHz. We therefore also looked at the measurement of residual ^{1}H–^{1}H dipolar couplings by DQ MAS NMR. This experiment has the advantage of usually good sensitivity due to the high natural abundance and gyromagnetic ratio of protons, and for highly mobile systems such as the LC under study, good resolution is achieved with low MAS frequencies. Small ^{1}H–^{1}H dipolar couplings, as low as 100 Hz, are also accessible from DQ build-up curves.

A 2D ^{1}H DQ–^{1}H SQ MAS NMR spectrum of CAGE-octanoic acid recorded at a MAS frequency of 5 kHz is presented in Figure 8. The excitation and reconversion of DQ coherence was achieved

using the POST-C7[53] recoupling sequence. The 2D DQ spectrum correlates the single-quantum (SQ) chemical shifts of the constituents of the dipolar coupled spin pair with the chemical shift of the DQ coherence that is equal to the sum of the chemical shifts of the coupled spins. The alkene protons of the geranic acid (H-2 and H-6), the choline methylene protons (H-1′ and H-2′) and H-8″ are resolved and there are three distinct resonances for the remaining aliphatic protons, with overlap of the octanoic acid aliphatic protons (H-4″, 5″, 6″, 7″), protons H-2″, H-4, H-5 and H-9 and the terminal methyl protons of geranic acid (H-8, H-10) with H-3″. The COOH/OH proton and the choline methyl protons (H-3′) are absent from the spectrum (see Figure S11 for full spectral range), indicating that they lack $^{1}H–^{1}H$ RDCs, consistent with our observations of high mobility from $^{1}H–^{13}C$ CP MAS NMR experiments. The highest intensity peaks are the auto DQ cross-peaks between like-spins (*i.e.* protons within CH_2 and methyl groups) for all resonances excluding the alkene protons, for which DQ peaks are observed to the aliphatic region (H-2 to H-4 and H-6 to H-8 at 5.7 + 2.1 = 7.8 and 5.1 + 1.7 = 6.8 ppm, respectively).

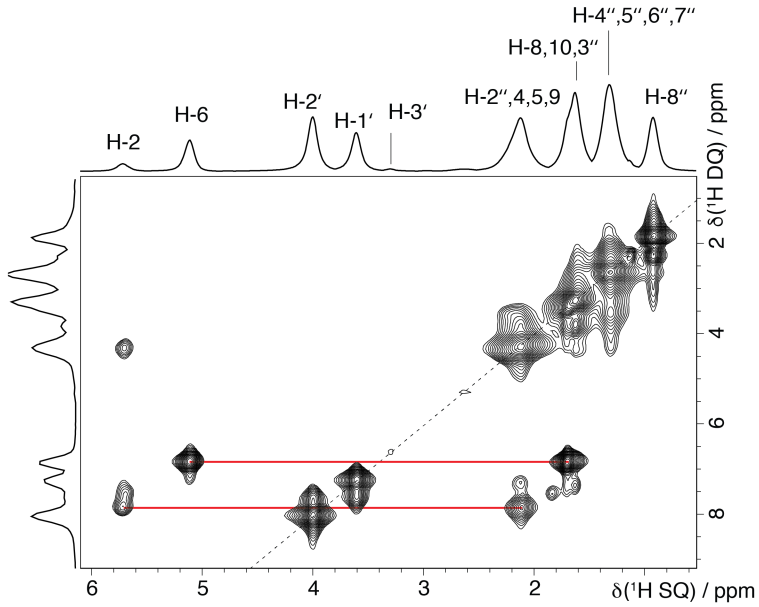

Figure 8. A ^{1}H DQ–^{1}H SQ MAS NMR spectrum (ν_{0H} = 500 MHz, ν_r = 5 kHz) with skyline projections of CAGE-oct, recorded with POST-C7 recoupling for τ_{DQ} = 1.2 ms (n_{rcpl} = 21) at 273 K. The base contour level is at 2.4% of the maximum peak intensity. For all methylene and methyl protons, the dominant dipolar coupling is the auto coupling between like spins along the diagonal (dashed line), whilst the dominant couplings of the CH protons (H-2 to H-4 and H-6 to H-8) are shown by solid red lines.

The partially averaged ^{1}H–^{1}H dipolar couplings report on the amplitude of fast motions of the internuclear vector. The ^{1}H–^{1}H dipolar couplings and corresponding order parameters, S_{HH}, also offer complementary insight due to the different angle between the dipolar coupling and rotation axis as compared to ^{1}H–^{13}C. In order to extract the ^{1}H–^{1}H dipolar coupling constants, and the related order parameter, S_{HH}, DQ build-up curves were recorded by incrementing the τ_{DQ} of the excitation and reconversion blocks (see pulse sequence in Figure 9a). Whilst relative dipolar couplings are accessible from the build-up of the DQ intensity,[98] intensity normalization is

necessary to obtain absolute values of the dipolar coupling.[31, 99] This is achieved by recording a second analogous reference experiment, without the selection of DQ coherences by omitting the receiver phase alternation (for further phase cycling details see Section 2.5).[34, 99] The sum of the DQ (I_{DQ}) and reference intensities (I_{ref}) is termed the multiple-quantum sum intensity, $I_{\Sigma MQ} = I_{DQ} + I_{ref}$.[34, 99] The effect of relaxation is removed from the DQ build-up by dividing the DQ intensity by the multiple-quantum sum intensity:

$$I_{nDQ} = \frac{I_{DQ}}{I_{\Sigma MQ}} \quad (1)$$

It is expected that, in the long-time limit, $I_{DQ} = I_{ref}$, and the normalized intensity, I_{nDQ}, should therefore reach a plateau value of 0.5.[99] The normalized DQ build-up curves may be fit using an inverted-Gaussian function derived using the second-moment approximation:[41-42, 99-100]

$$I_{nDQ} = \tfrac{1}{2}\left(1 - \exp\left\{-kD_{res}^2\tau_{DQ}^2\right\}\right) \qquad (2)$$

Where, for the case of a multiple spin system, the residual dipolar coupling represents an average second-moment-type quantity:[101]

$$D_{res} = \left(\sum\nolimits_{pairs} D^2\right)^{1/2} \quad (3)$$

The scaling factor, k, in Equation (2) is pulse-sequence specific and $k_{C7} = 0.86/15 \approx 0.057$ for POST-C7.[102] Equation (2) can only fit the initial build-up region up to $I_{nDQ} \leq 0.45$.[103] An improved analysis of ^{1}H DQ build-up curves was demonstrated using the 'Abragam-like' (A-l) build-up function, derived empirically from data on different elastomers:[104]

$$I_{nDQ} = \tfrac{1}{2}\left(1 - \exp\left[-\left\{0.143D_{res}\tau_{DQ}\right\}^{1.5}\right] \times \cos\left[0.221D_{res}\tau_{DQ}\right]\right) \qquad (4)$$

Note that the empirical factors in Equation (4) have been adjusted to take into account the scaling factor for POST-C7 recoupling, compared to those previously reported for the static case.[104] The

A-l function extends the fitting range for DQ build-up curves, enabling fitting of the local maximum, extending above 0.5, which is pronounced in systems with a narrow RDC distribution.[99] For samples with a wide distribution of RDCs, the maximum vanishes, and Equation (4) may be combined with a distribution of RDCs.[104]

I_{DQ}, I_{ref} and I_{nDQ} for a representative peak at 1.3 ppm due to the octanoic acid alkyl chain protons H-4″–7″, are shown in Figure 9b. The normalized DQ build-up curves for all ^{1}H peaks of CAGE-oct are shown in Figure 9c. The build-up curves do not reach the expected plateau level of 0.5 for any of the protons. This effect has previously been observed for elastomer systems and attributed to isotropically mobile components (short dangling chains and solvent molecules).[99] Such liquid-like components contribute to the reference intensity, but not I_{DQ} (as they lack RDCs), meaning that the normalized intensity, I_{nDQ}, will be lower than expected. In some cases, it has been demonstrated that these components form more slowly relaxing long-time tails of I_{ref} which may be fit to an exponential and subtracted to produce a well-behaving normalized build-up curve reaching the 50% intensity plateau.[99] For CAGE-oct, the long-time relaxing component is similar in both the DQ and reference intensity (Figure 9b), and it was therefore not possible to unambiguously subtract an exponential tail from the reference curve. A method to solve this problem is based on the fact that in the long-time limit, where $I_{DQ} = I_{ref}$, the more mobile fraction may be identified and fitted in a plot of $I_{ref} - I_{DQ}$ vs. τ_{DQ} (Figure S12).[105] Figure 9d shows the normalized build-up curves with the long-time exponential tail subtracted from the reference curve in this way (see Figure S12), which reach the expected plateau of 0.5. Most of the build-up curves show a pronounced maximum, indicative of a narrow RDC distribution. The build-up curves were fitted to Equation (4) and the values of D_{res}, which range from 0.5 to 3.7 kHz, are given in Table 2.

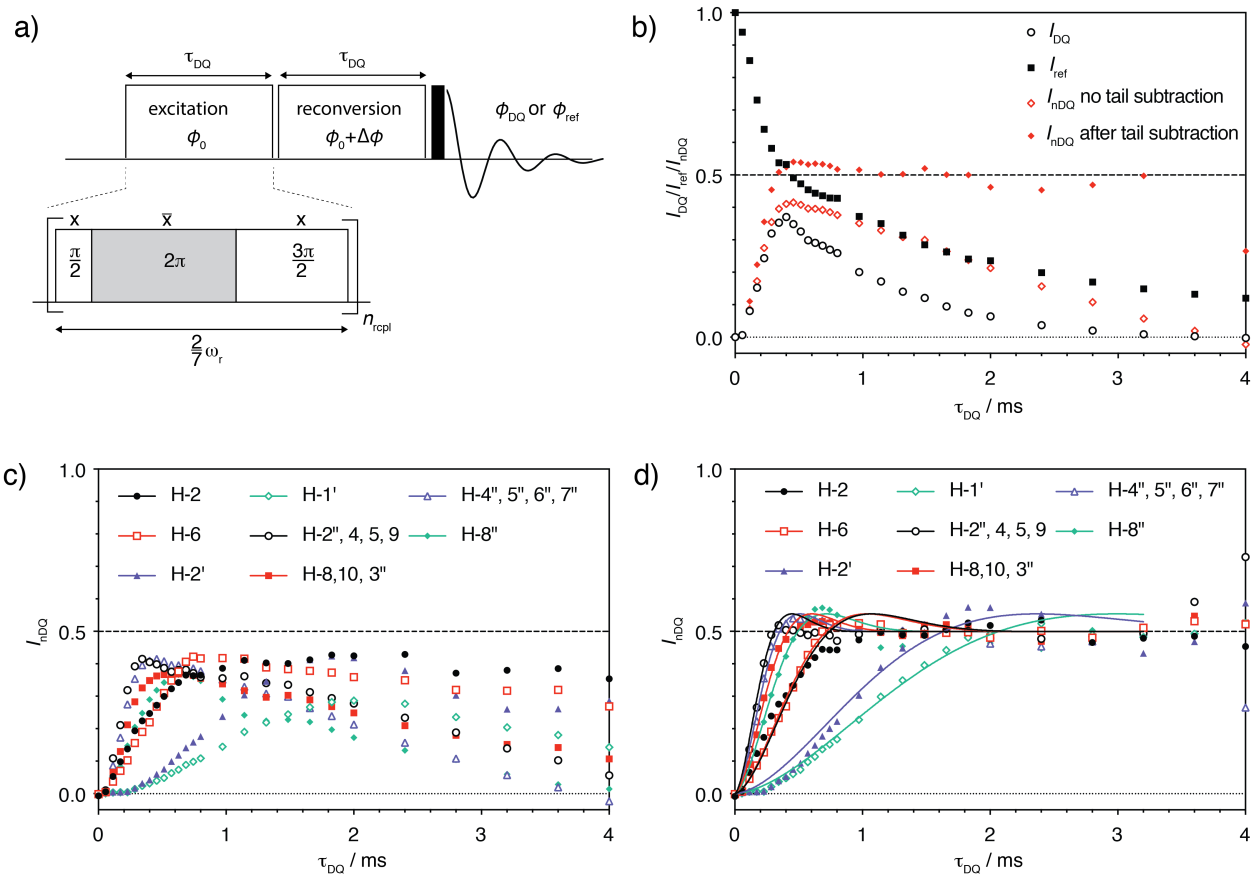

Figure 9. (a) Pulse sequences used to measure ^{1}H DQ build-up curves (see discussion in Section 2.5 of the use of phase cycling to record the I_{DQ} and I_{ref} signals). (b) DQ (I_{DQ}), reference (I_{ref}) and normalized DQ intensity (I_{nDQ}, see Equation 1) with and without tail subtraction for a representative peak (H-4″–7″, 1.3 ppm) of CAGE-oct. (c, d) Normalized ^{1}H DQ build-up curves for all resolved ^{1}H peaks of CAGE-oct recorded with no tail subtraction (c) or with tail subtraction (d). The solid lines in (d) are fits to the A-l build-up function (Equation 4) up to τ_{DQ} = 3.2 ms.

Table 2. Results of fits of the experimental ^{1}H DQ build-curves (Figure 9d, recorded at 273 K) to the A-l build-up function (Equation 4).

Peak	Dominant coupling	$D_{res}/2\pi$ / kHz	S_{HH}
H-2″, 4, 5, 9	CH_2 auto	3.7 ± 0.1	0.173 ± 0.007
H-4″, 5″, 6″, 7″	CH_2 auto	3.21 ± 0.07	0.151 ± 0.003
H-8″	Methyl auto	2.29 ± 0.06	0.151 ± 0.004
H-2	H-4 (CH to CH_2)	1.53 ± 0.06	0.151 ± 0.006
H-6	H-8 (CH to CH_3)	1.58 ± 0.03	0.144 ± 0.002
H-8, 10, 3″	CH_2 auto	2.72 ± 0.06	0.128 ± 0.003
H-2′	CH_2 auto	0.69 ± 0.02	0.032 ± 0.001
H-1′	CH_2 auto	0.546 ± 0.009	0.0257 ± 0.0004
H-3′	–[a]	–[a]	–[a]
COOH/OH	–[a]	–[a]	–[a]

[a]No build-up of DQ coherence was detected

In order to probe whether the lower than expected plateau (Figure 9c) is a result of liquid-like signal contributions (*i.e.*, lacking orientational order), we applied the experimental approach of DQ pre-selection. Saalwächter *et al.* introduced this strategy as a means to suppress such unwanted contributions arising from dangling chain ends and solvent molecules in polymer networks, as an alternative to the exponential tail correction.[99] This strategy involves applying an additional fixed DQ excitation/reconversion block, followed by a z-filter delay, τ_z, preceding the incremented DQ pulse sequence of the original experiment (Figure S13a). The first block acts as a DQ pre-selection filter such that only dipolar-coupled components are selected. Application of the pre-selection filter results in an increased intensity of the DQ build-up curve relative to the reference curve (Figure S13b, c). The resulting normalized curves reach a maximum value of between 15 to 26%

higher than the curves recorded with no DQ pre-selection filter and are significantly closer to reaching the expected plateau of 0.5. Fits to Equation (2) give $D_{res}/2\pi$ values comparable to those obtained from fits to data recorded without DQ pre-selection, following tail subtraction (Table S3). The difference between the DQ build-up curves with and without DQ pre-selection suggests that, within the liquid crystalline sample, there are some less ordered components (either unordered regions or individual ions/clusters within the ordered phase) that do not have RDCs or have very small RDCs and justifies the subtraction of the long-time tail from the data recorded with no DQ pre-selection. Further evidence of an isotropic component is provided by $^{1}H–^{13}C$ DIPSHIFT experiments recorded with either direct polarization or $^{1}H–^{13}C$ CP, given in the SI (Figure S10b, Table S2 and additional discussion in Section S4.2). We estimated a disordered component of approximately 23%, in agreement with our observations from ^{1}H DQ build-up experiments, and the presence of isotropic regions observed by polarizing optical microscopy. The coexistence of liquid disordered/liquid ordered phases has previously been reported in a model membrane system and quantified by $^{1}H–^{13}C$ dipolar coupling MAS NMR.[106]

3.8 S_{CH} and S_{HH} Order Parameters

Order parameters, S_{CH} and S_{HH}, were calculated as the ratio of the motionally averaged dipolar coupling to the rigid limit value and are reported in Table 1 and 2, respectively. The order parameters are assigned a color based on their range to show the structural correlation in Figure 10a (S_{CH}) and b (S_{HH}). Since the dipolar coupling depends on orientation according to $\frac{1}{2}(3\cos^2\theta - 1)$ (see Section S1), S reports on the amplitude of fast motions (of the ions and molecular segments/bonds). S_{CH} ranged from ~0 to 0.224 while S_{HH} ranged from ~0 to 0.173 (in comparison to $S = 1$ for a rigid system). These order parameters are significantly lower compared to those of smectic phases of non-ionic LCs, which typically display order parameters of 0.4-0.8[107-109] and are

rather similar to those reported for lamellar phases formed by lyotropic mesogen/solvent systems.[110-112] Highly disordered alkyl chains corresponding to low orientational order parameters have been found for other ILCs.[15, 45-46, 113] The differences in order parameters between conventional non-ionic LCs and ILCs such as CAGE-oct can be attributed to differences in the molecular structures and nature of the intermolecular interactions which are the driving forces for mesophase formation. Non-ionic LCs typically contain a rigid (usually aromatic) core and one or more flexible chains, with the LC phase stabilized by dispersion forces.[3] ILCs on the other hand consist of ions, one of which usually contains a long ($n > 8$) alkyl chain, and typically form smectic phases stabilized by electrostatic (Coulombic) interactions within ion-rich layers, and, in some cases (likely the case for CAGE-oct), hydrogen bonding.[93]

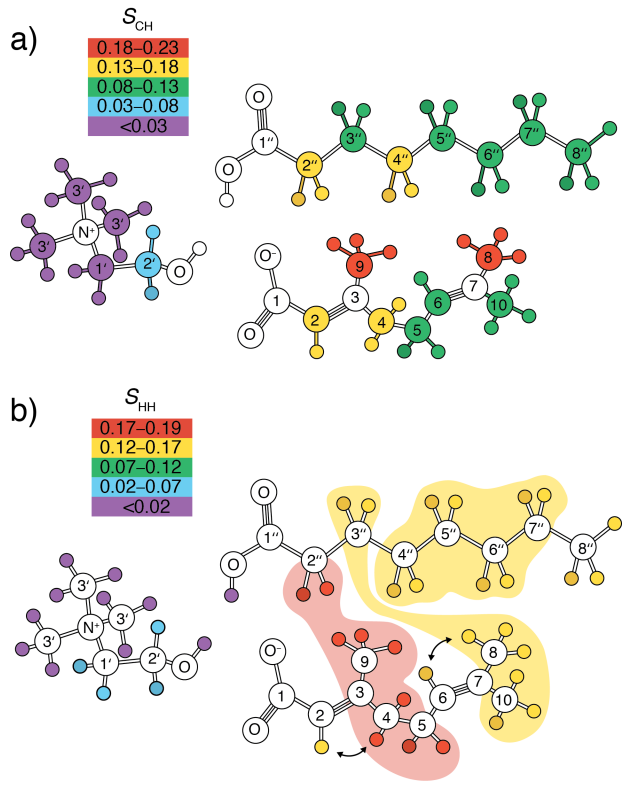

Figure 10. Schematic representation of site-specific order parameters, (a) S_{CH} and (b) S_{HH}. In (a), S_{CH} is the order parameter for each carbon and its covalently bonded proton(s) determined by CP build-up curves. In (b), S_{HH} is the order parameter between protons within individual methylene or methyl groups, apart from H-2 and H-6, for which the dominant dipolar couplings are shown by arrows. The highlighted groups of protons in (b) indicate protons with overlapping peaks in the 1D ^{1}H MAS NMR spectrum (see Figure 4a), and as such only a single S_{HH} was determined for these groups of protons.

Distinct motional amplitudes were observed between the choline cation compared to the anions, and also within the ions. From the trends in these order parameters, conclusions on the structure as well as dynamics can be drawn. Choline showed lower order parameters compared to those of geranate and octanoate, indicating increased mobility. Of the choline carbons, the CH_2 adjacent to

the hydroxyl group, C-2′, showed the highest order parameter, S_{CH} = 0.039. In comparison, the adjacent CH_2 group, C-1′, and the choline methyl group, C-3′, showed much smaller dipolar couplings, indicating nearly isotropic freedom of motion (S_{CH} ~ 0) of the choline head group. The $^1H–^1H$ RDC for the choline methylene group H-1′ for which the corresponding $^1H–^{13}C$ RDC was too low to accurately determine from the CP build-up curves, was determined to be 546 Hz, corresponding to S_{HH} = 0.0257. We note that the calculated order parameters consider only the dominant dipolar coupling, the auto coupling between the methylene protons, for D_{rigid}, whilst the measured RDC is an averaged value of all couplings. Taking into account the additional weak coupling between the H-1′ and H-2′ protons on adjacent methylene groups, as observed in the 2D ^1H DQ–^1H SQ NMR spectra would result in only a very slight reduction of S_{HH}. The trend in S_{HH} for the choline protons, increasing from S_{HH} = ~0 (H-3′; no build-up of DQ coherences observed) to 0.0257 (H-1′) and 0.032 (H-2′) agrees with our conclusions based on the $^1H–^{13}C$ RDCs exhibiting an increasing degree of motion from the hydroxyl group to the $–N(CH_3)_3$ head group. The hydroxyl end of the molecule is likely ‘anchored’ by hydrogen bonding to the geranate and octanoate. This suggests that hydrogen bonding between all three constituent parts, rather than a purely electrostatic interaction, is critical to understanding the structure of CAGE-oct, consistent with strong evidence of hydrogen bonded [(choline)(geranate)(H)(octanoate)], [(choline)$(octanoate)_2$(H)] and [(choline)$(geranate)_2$)(H)] clusters from mass spectrometry and ^1H MAS NMR. The choline head group can be envisioned to reorient as it changes hydrogen bonding partners in the dynamic smectic phase. The order parameters are comparable to those obtained for the choline head group in aqueous phospholipid lamellar phases. For example, Hong *et al.* reported S_{CH} values for the choline head group of phosphatidylcholine (PC) in the fluid lamellar (L_α) phase of magnitude 0.005 (γ; corresponding to C-3′) and 0.04 (α and β; corresponding to C-3′ and C-

2′),[111, 114] corresponding to purple and blue, respectively, on the scale in Figure 10a. Notably, the choline head group is covalently attached via the oxygen in PC, yet the adjacent α proton displays a remarkably similar order parameter to the equivalent C-2′ of the 'free' choline in CAGE-oct (S_{CH} = 0.04 and 0.039), further suggesting strong hydrogen-bonding of the choline cation to geranate/octanoate.

The S_{CH} of the aliphatic chain protons of geranate and octanoate are generally lower at the terminal end compared to those closest to the carboxylic acid group. S_{CH} of the methylene groups of octanoic acid vary between 0.174 at C-2″ to 0.082 at C-7″, whilst those of the geranate backbone show similar values and are again slightly higher at the backbone carbons closest to the carboxyl group (C-2 and C-4, compared to C-6 and C-10; Figure 10a). The methyl groups branching from the main chain of geranic acid, C-9 and C-8, have the highest S_{CH}, which could result from the C–H vectors being more closely aligned with the long molecular axis of geranic acid, which would result in the least averaging due to axial rotation of the molecule about the long axis. The S_{HH} for the overlapping octanoic acid alkyl chain protons H-4″–7″ of 0.151 is close to the highest S_{CH} obtained for these carbons (S_{CH} = 0.136 for C-4″), as expected since the strongest dipolar couplings will dominate the build-up of DQ coherences. The S_{HH} of 0.173 for protons H-2″, 4, 5 and 9 agrees with S_{CH} of 0.174 of C-2″. The S_{HH} of the terminal methyl group of octanoate (H-8″) is 0.151, compared to S_{CH} of 0.120. As for choline, the order parameters of the alkyl chains resemble those of lyotropic phospholipid systems; which range from ~0.24 to 0.02 along the acyl tail of PC in the L_α phase (corresponding to red to purple, on the scale in Figure 10a).[114] Overall, for CAGE-oct, S_{HH} and S_{CH} are observed to provide the same information about the dynamics of the system (Figure 10a). The order parameters, S_{CH}, reported above at 273 K, do not change significantly at lower temperatures (243 and 253 K; Figure S14).

4. Conclusions

In this work, a neat system, based on choline, geranic acid and octanoic acid has been investigated by MAS NMR, SAXS, polarizing optical microscopy, and mass spectrometry. At temperatures below ~293 K, CAGE-oct forms a mobile bilayer liquid-crystalline phase. Mass spectrometry reveals the presence of $[(\text{choline})(\text{geranate})(\text{octanoate})]^-$, $[(\text{choline})(\text{octanoate})_2]^-$ and $[(\text{choline})(\text{geranate})_2]^-$ species at intensities significantly higher than expected of electrostatic ion clusters when compared to those for $[(\text{anion})_2]^-$ species, suggesting strong association of the choline cation with the anions. ^{1}H MAS NMR suggests that these species are hydrogen bonded clusters, with hydrogen bonds involving the carboxylic acid, carboxylate and hydroxyl groups. The hydrogen bonding is dynamic, with both anion metathesis and hydrogen exchange taking place, resulting in averaging of the ^{1}H chemical shifts. The temperature dependence of the ^{1}H chemical shifts suggests that a similar hydrogen bonding arrangement occurs in both the isotropic and LC phases.

The CAGE-oct ILC was further investigated by means of MAS NMR spectroscopy which provides information about the mobility and degree of ordering of the individual ions and molecular segments which is not accessible from other techniques such as SAXS. The dynamic order parameters, S_{CH} and S_{HH}, in the range 0 to 0.2, indicate a highly mobile LC phase, with the obtained ordered parameters being considerably lower than those reported for typical non-ionic LCs, and instead resembling those of aqueous phospholipid bilayer systems. The increased mobility toward the terminal ends of geranate and octanoate alkyl chains, and the choline $-N(CH_3)_3$ head-group are consistent with hydrogen bonding of the choline cation and anions and indicate that the CAGE-oct LC consists of mobile ionic-rich layers, and regions of fluid alkyl chains. The coexistence of an isotropic component (approximately 25% of the sample) was also

detected within the LC with phase. This present work shows that MAS NMR is a highly promising tool for studying the site-specific structure and dynamics of mesogens, utilizing heteronuclear techniques such as the build-up in $^{1}H–^{13}C$ CP or ^{1}H DQ MAS NMR experiments.

ASSOCIATED CONTENT

Electronic Supplementary Information (ESI) available: Additional details on the dipolar coupling and order parameter; additional spectroscopic characterization (solution phase ^{1}H and $^{13}C\{^{1}H\}$ NMR spectra, IR spectrum and mass spectra); additional experimental details; determination of 95% confidence intervals for D_{CH}; temperature dependence of the layer repeat distance; polarizing optical micrographs; $^{1}H–^{13}C$ HETCOR MAS NMR spectrum; additional MAS NMR discussion; further fits of experimental $^{1}H–^{13}C$ CP build-up curves; effect of proton-proton dipolar couplings on simulated CP build-up curves; DIPSHIFT profiles; ^{1}H DQ–^{1}H SQ MAS NMR spectrum; plots of $I_{ref}–I_{DQ}$; ^{1}H DQ build-up curves recorded with DQ pre-selection; temperature dependence of S_{CH}; example SIMPSON input files.

AUTHOR INFORMATION

Corresponding Authors

*E-mail: S.P.Brown@warwick.ac.uk; J.R.Lewandowski@warwick.ac.uk

Present Addresses

† Department of Chemistry, Britannia House, King's College London, London, SE1 1DB, U.K

Author Contributions

The manuscript was written through contributions of all authors. All authors have given approval to the final version of the manuscript.

ACKNOWLEDGMENT

Funding from GSK for the Engineering Medicines Laboratory at Imperial and a PhD studentship (SKM) is acknowledged. SKM is supported by a University of Warwick International Chancellor's scholarship. JRL acknowledges funding from ERC Starting Grant 639907 and BBSRC grant BB/R010218/1. Andrew Edwards, Bernie O'Hare, Andrew Tatton and Dewey Barich (GSK) are thanked for discussions of the NMR results. Kay Saalwächter is acknowledged for valuable discussions. The data for this study is provided as a supporting dataset from WRAP, the Warwick Research Archive Portal at http://wrap.warwick.ac.uk/*****/.

ABBREVIATIONS

A-l, Abragam-like; CAGE, choline and geranate; CAGE-oct, CAGE octanoic acid; CP, cross-polarization; DES, deep eutectic solvent; DIPSHIFT, dipolar-chemical shift correlation; DP, direct polarization; DQ, double-quantum; FSLG, frequency-switched Lee-Goldburg; HETCOR, heteronuclear correlation; IL, ionic liquid; ILC, ionic liquid crystal; LC, liquid crystal; MAS, magic-angle spinning; NMR, nuclear magnetic resonance; RDC, residual dipolar coupling; RSS, residual sum of square; SAXS, small-angle X-ray scattering; SQ, single-quantum; TMS, tetramethylsilane; TC, temperature coefficient.

REFERENCES

1. Wasserscheid, P.; Welton, T., Ionic Liquids in Synthesis. In *Ionic Liquids in Synthesis*, Second ed.; Wiley-VCH: Weinheim, 2003.

2. Wilkes, J. S., A Short History of Ionic Liquids—from Molten Salts to Neoteric Solvents. *Green Chemistry* **2002,** *4*, 73-80.

3. Goossens, K.; Lava, K.; Bielawski, C. W.; Binnemans, K., Ionic Liquid Crystals: Versatile Materials. *Chem. Rev.* **2016,** *116*, 4643-4807.

4. Axenov, K. V.; Laschat, S., Thermotropic Ionic Liquid Crystals. *Materials* **2011,** *4*, 206-259.

5. Alvarez Fernandez, A.; Kouwer, H. P., Key Developments in Ionic Liquid Crystals. *Int. J. Mol. Sci.* **2016,** *17*, 731.

6. Schadt, M., Liquid Crystal Materials and Liquid Crystal Displays. *Annu. Rev. Mater. Sci.* **1997,** *27*, 305-379.

7. Costa, R. D.; Werner, F.; Wang, X.; Grönninger, P.; Feihl, S.; Kohler, F. T. U.; Wasserscheid, P.; Hibler, S.; Beranek, R.; Meyer, K., et al., Beneficial Effects of Liquid Crystalline Phases in Solid-State Dye-Sensitized Solar Cells. *Adv. Energy Mater.* **2013,** *3*, 657-665.

8. Yamanaka, N.; Kawano, R.; Kubo, W.; Kitamura, T.; Wada, Y.; Watanabe, M.; Yanagida, S., Ionic Liquid Crystal as a Hole Transport Layer of Dye-Sensitized Solar Cells. *Chem. Commun.* **2005**, 740-742.

9. Yamanaka, N.; Kawano, R.; Kubo, W.; Masaki, N.; Kitamura, T.; Wada, Y.; Watanabe, M.; Yanagida, S., Dye-Sensitized TiO_2 Solar Cells Using Imidazolium-Type Ionic Liquid Crystal Systems as Effective Electrolytes. *J. Phys. Chem. B* **2007,** *111*, 4763-4769.

10. Lee, C. K.; Huang, H. W.; Lin, I. J. B., Simple Amphiphilic Liquid Crystalline N-Alkylimidazolium Salts. A New Solvent System Providing a Partially Ordered Environment. *Chem. Commun.* **2000**, 1911-1912.

11. Bruce, D. W.; Gao, Y.; Canongia Lopes, J. N.; Shimizu, K.; Slattery, J. M., Liquid-Crystalline Ionic Liquids as Ordered Reaction Media for the Diels–Alder Reaction. *Chem. Eur. J* **2016,** *22*, 16113-16123.

12. Taubert, A., CuCl Nanoplatelets from an Ionic Liquid-Crystal Precursor. *Angew. Chem., Int. Ed.* **2004,** *43*, 5380-5382.

13. Neidhardt, M. M.; Schmitt, K.; Baro, A.; Schneider, C.; Bilitewski, U.; Laschat, S., Self-Assembly and Biological Activities of Ionic Liquid Crystals Derived from Aromatic Amino Acids. *Phys. Chem. Chem. Phys.* **2018,** *20*, 20371-20381.

14. Dobbs, W.; Heinrich, B.; Bourgogne, C.; Donnio, B.; Terazzi, E.; Bonnet, M.-E.; Stock, F.; Erbacher, P.; Bolcato-Bellemin, A.-L.; Douce, L., Mesomorphic Imidazolium Salts: New Vectors for Efficient siRNA Transfection. *J. Am. Chem. Soc.* **2009,** *131*, 13338-13346.

15. Dai, J.; Kharkov, B.; Dvinskikh, S., Molecular and Segmental Orientational Order in a Smectic Mesophase of a Thermotropic Ionic Liquid Crystal. *Crystals* **2018,** *9*, 18.

16. Douliez, J.-P.; Ferrarini, A.; Dufourc, E.-J., On the Relationship Between C-C and C-D Order Parameters and Its Use for Studying the Conformation of Lipid Acyl Chains in Biomembranes. *J. Chem. Phys* **1998,** *109*, 2513-2518.

17. Zakrewsky, M.; Banerjee, A.; Apte, S.; Kern, T. L.; Jones, M. R.; Sesto, R. E. D.; Koppisch, A. T.; Fox, D. T.; Mitragotri, S., Choline and Geranate Deep Eutectic Solvent as a Broad-Spectrum Antiseptic Agent for Preventive and Therapeutic Applications. *Adv. Healthcare Mater.* **2016,** *5*, 1282-1289.

18. Banerjee, A.; Ibsen, K.; Iwao, Y.; Zakrewsky, M.; Mitragotri, S., Transdermal Protein Delivery Using Choline and Geranate (CAGE) Deep Eutectic Solvent. *Adv. Healthcare Mater.* **2017,** *6*, 1601411.

19. Zakrewsky, M.; Lovejoy, K. S.; Kern, T. L.; Miller, T. E.; Le, V.; Nagy, A.; Goumas, A. M.; Iyer, R. S.; Del Sesto, R. E.; Koppisch, A. T., et al., Ionic Liquids as a Class of Materials for Transdermal Delivery and Pathogen Neutralization. *Proc. Nat. Acad. Sc. U. S.* **2014,** *111*, 13313-13318.

20. Banerjee, A.; Ibsen, K.; Brown, T.; Chen, R.; Agatemor, C.; Mitragotri, S., Ionic Liquids for Oral Insulin Delivery. *Proc. Nat. Acad. Sc. U. S.* **2018,** *115*, 7296-7301.

21. Tanner, E. E. L.; Ibsen, K. N.; Mitragotri, S., Transdermal Insulin Delivery Using Choline-Based Ionic Liquids (CAGE). *Journal of Controlled Release* **2018,** *286*, 137-144.

22. Shi, Y.; Zhao, Z.; Gao, Y.; Pan, D. C.; Salinas, A. K.; Tanner, E. E. L.; Guo, J.; Mitragotri, S., Oral Delivery of Sorafenib Through Spontaneous Formation of Ionic Liquid Nanocomplexes. *Journal of Controlled Release* **2020,** *322*, 602-609.

23. Banerjee, A.; Ibsen, K.; Brown, T.; Chen, R.; Agatemor, C.; Mitragotri, S., Reply to Rogers and Gurau: Definitions of Ionic Liquids and Deep Eutectic Solvents. *Proc. Nat. Acad. Sc. U. S.* **2018,** *115*, E11000-E11001.

24. Calucci, L.; Veracini, C. A., Liquid Crystals and Liquid Crystal Solutions Studied by NMR. In *Encyclopedia of Spectroscopy and Spectrometry (Second Edition)*, Lindon, J. C., Ed. Academic Press: Oxford, 2010; pp 1349-1356.

25. Müller, L.; Kumar, A.; Baumann, T.; Ernst, R. R., Transient Oscillations in NMR Cross-Polarization Experiments in Solids. *Phys Rev Lett.* **1974,** *32*, 1402-1406.

26. Hong, M.; Yao, X.; Jakes, K.; Huster, D., Investigation of Molecular Motions by Lee-Goldburg Cross-Polarization NMR Spectroscopy. *J. Phys. Chem. B* **2002,** *106*, 7355-7364.

27. Nagaraja, C. S., Determination of Order Parameters of Liquid Crystals: Use of Dipolar Oscillations Enhanced by Lee-Goldburg Decoupling. *Liq. Cryst.* **1999,** *26*, 17-21.

28. Ramanathan, K. V.; Sinha, N., Ordering in Nematic Liquid Crystals from NMR Cross-Polarization Studies. *Pramana* **2003,** *61*, 249-262.

29. Brown, S. P.; Schnell, I.; Brand, J. D.; Müllen, K.; Spiess, H. W., An Investigation of π−π Packing in a Columnar Hexabenzocoronene by Fast Magic-Angle Spinning and Double-Quantum ^{1}H Solid-State NMR Spectroscopy. *J. Am. Chem. Soc.* **1999,** *121*, 6712-6718.

30. Brown, S. P.; Schnell, I.; Brand, J. D.; Müllen, K.; Spiess, H. W., A ^{1}H Double-Quantum Magic-Angle Spinning Solid-State NMR Investigation of Packing and Dynamics in Triphenylene and Hexabenzocoronene Derivatives. *J. Mol. Struct.* **2000,** *521*, 179-195.

31. Graf, R.; Heuer, A.; Spiess, H. W., Chain-Order Effects in Polymer Melts Probed by ^{1}H Double-Quantum NMR Spectroscopy. *Phys Rev Lett.* **1998,** *80*, 5738-5741.

32. Dollase, T.; Graf, R.; Heuer, A.; Spiess, H. W., Local Order and Chain Dynamics in Molten Polymer Blocks Revealed by Proton Double-Quantum NMR. *Macromolecules* **2001,** *34*, 298-309.

33. Saalwächter, K., An Investigation of Poly(dimethylsiloxane) Chain Dynamics and Order in Its Inclusion Compound with γ-Cyclodextrin by Fast-MAS Solid-State NMR Spectroscopy. *Macromol. Rapid Commun.* **2002,** *23*, 286-291.

34. Saalwächter, K., Methyl Groups as Local Probes for Polymer Dynamics as Investigated by ^{1}H Double-Quantum Magic-Angle Spinning NMR Spectroscopy. *Chem. Phys. Lett.* **2002,** *362*, 331-340.

35. Schneider, M.; Gasper, L.; Demco, D. E.; Blümich, B., Residual Dipolar Couplings by ^{1}H Dipolar-Encoded Longitudinal Magnetization, Double- and Triple-Quantum Nuclear Magnetic Resonance in Cross-Linked Elastomers. *J. Chem. Phys* **1999,** *111*, 402-415.

36. Geen, H.; Titman, J. J.; Gottwald, J.; Spiess, H. W., Solid-State Proton Multiple-Quantum NMR Spectroscopy with Fast Magic Angle Spinning. *Chem. Phys. Lett.* **1994,** *227*, 79-86.

37. Gottwald, J.; Demco, D. E.; Graf, R.; Spiess, H. W., High-Resolution Double-Quantum NMR Spectroscopy of Homonuclear Spin Pairs and Proton Connectivities in Solids. *Chem. Phys. Lett.* **1995,** *243*, 314-323.

38. Brown, S. P.; Spiess, H. W., Advanced Solid-State NMR Methods for the Elucidation of Structure and Dynamics of Molecular, Macromolecular, and Supramolecular Systems. *Chem. Rev.* **2001,** *101*, 4125-4156.

39. Brown, S. P., Probing Proton–Proton Proximities in the Solid State. *Prog. Nucl. Magn. Reson. Spectrosc.* **2007,** *50*, 199-251.

40. Brown, S. P., Applications of High-Resolution ^{1}H Solid-State NMR. *Solid State Nucl. Magn. Reson.* **2012,** *41*, 1-27.

41. Saalwächter, K.; Heuer, A., Chain Dynamics in Elastomers As Investigated by Proton Multiple-Quantum NMR. *Macromolecules* **2006,** *39*, 3291-3303.

42. Saalwächter, K.; Herrero, B.; López-Manchado, M. A., Chain Order and Cross-Link Density of Elastomers As Investigated by Proton Multiple-Quantum NMR. *Macromolecules* **2005,** *38*, 9650-9660.

43. Fernando Cobo, M.; Maliňáková, K.; Reichert, D.; Saalwächter, K.; Ribeiro deAzevedo, E., Intermediate Motions and Dipolar Couplings as Studied by Lee–Goldburg Cross-Polarization NMR: Hartmann–Hahn Matching Profiles. *Phys. Chem. Chem. Phys.* **2009,** *11*, 7036-7047.

44. Achilles, A.; Bärenwald, R.; Lechner, B.-D.; Werner, S.; Ebert, H.; Tschierske, C.; Blume, A.; Bacia, K.; Saalwächter, K., Self-Assembly of X-Shaped Bolapolyphiles in Lipid Membranes: Solid-State NMR Investigations. *Langmuir.* **2016,** *32*, 673-682.

45. Di Pietro, M. E.; Margola, T.; Celebre, G.; De Luca, G.; Saielli, G., A Combined LX-NMR and Molecular Dynamics Investigation of the Bulk and Local Structure of Ionic Liquid Crystals. *Soft Matter* **2019,** *15*, 4486-4497.

46. Dai, J.; Majhi, D.; Kharkov, B. B.; Dvinskikh, S. V., NMR Spectroscopic Study of Orientational Order in Imidazolium-Based Ionic Liquid Crystals. *Crystals* **2019,** *9*, 495.

47. Schneider, C. A.; Rasband, W. S.; Eliceiri, K. W., NIH Image to ImageJ: 25 Years of Image Analysis. *Nature methods* **2012,** *9*, 671-675.

48. Metz, G.; Ziliox, M.; Smith, S. O., Towards Quantitative CP-MAS NMR. *Solid State Nucl. Magn. Reson.* **1996,** *7*, 155-160.

49. Marion, D.; Ikura, M.; Tschudin, R.; Bax, A., Rapid Recording of 2D NMR Spectra Without Phase Cycling. Application to the Study of Hydrogen Exchange in Proteins. *Journal of Magnetic Resonance (1969)* **1989,** *85*, 393-399.

50. Fung, B. M.; Khitrin, A. K.; Ermolaev, K., An Improved Broadband Decoupling Sequence for Liquid Crystals and Solids. *J. Magn. Reson* **2000,** *142*, 97-101.

51. Lee, M.; Goldburg, W. I., Nuclear-Magnetic-Resonance Line Narrowing by a Rotating rf Field. *Phys. Rev.* **1965,** *140*, A1261-A1271.

52. Bielecki, A.; Kolbert, A. C.; De Groot, H. J. M.; Griffin, R. G.; Levitt, M. H., Frequency-Switched Lee—Goldburg Sequences in Solids. In *Advances in Magnetic and Optical Resonance*, Warren, W. S., Ed. Academic Press: 1990; Vol. 14, pp 111-124.

53. Hohwy, M.; Jakobsen, H. J.; Edén, M.; Levitt, M. H.; Nielsen, N. C., Broadband dipolar recoupling in the nuclear magnetic resonance of rotating solids: A compensated C7 pulse sequence. *J. Chem. Phys.* **1998,** *108*, 2686-2694.

54. Hayashi, S.; Hayamizu, K., Chemical Shift Standards in High-Resolution Solid-State NMR (1) ^{13}C, ^{29}Si, and ^{1}H Nuclei. *Bulletin of the Chemical Society of Japan* **1991,** *64*, 685-687.

55. Morcombe, C. R.; Zilm, K. W., Chemical Shift Referencing in MAS Solid State NMR. *J. Magn. Reson* **2003,** *162*, 479-486.

56. Bak, M.; Rasmussen, J. T.; Nielsen, N. C., SIMPSON: A General Simulation Program for Solid-State NMR Spectroscopy. *J. Magn. Reson* **2000,** *147*, 296-330.

57. Tošner, Z.; Andersen, R.; Stevensson, B.; Edén, M.; Nielsen, N. C.; Vosegaard, T., Computer-Intensive Simulation of Solid-State NMR Experiments using SIMPSON. *J. Magn. Reson* **2014,** *246*, 79-93.

58. Beale, E. M. L., Confidence Regions in Non-Linear Estimation. *J. Royal Stat. Soc. Ser. B* **1960,** *22*, 41-76.

59. Seber, G. A. F.; Wild, C. J., Nonlinear Regression. Wiley-Interscience: Hoboken, USA, 2003.

60. Barrick, D., Biomolecular Thermodynamics: From Theory to Application. CRC Press: Boca Raton, Florida, 2014.

61. Binnemans, K., Ionic Liquid Crystals. *Chem. Rev.* **2005,** *105*, 4148-4204.

62. Saielli, G., Special Issue Editorial: Ionic Liquid Crystals. *Crystals* **2019,** *9*, 274.

63. Saielli, G.; Satoh, K., A Coarse-Grained Model of Ionic Liquid Crystals: The Effect of Stoichiometry on the Stability of the Ionic Nematic Phase. *Phys. Chem. Chem. Phys.* **2019,** *21*, 20327-20337.

64. Triolo, A.; Russina, O.; Bleif, H.-J.; Di Cola, E., Nanoscale Segregation in Room Temperature Ionic Liquids. *J. Phys. Chem. B* **2007,** *111*, 4641-4644.

65. Triolo, A.; Russina, O.; Fazio, B.; Triolo, R.; Di Cola, E., Morphology of 1-Alkyl-3-Methylimidazolium Hexafluorophosphate Room Temperature Ionic Liquids. *Chem. Phys. Lett.* **2008,** *457*, 362-365.

66. Greaves, T. L.; Kennedy, D. F.; Mudie, S. T.; Drummond, C. J., Diversity Observed in the Nanostructure of Protic Ionic Liquids. *J. Phys. Chem. B* **2010,** *114*, 10022-10031.

67. Russina, O.; Lo Celso, F.; Di Michiel, M.; Passerini, S.; Appetecchi, G. B.; Castiglione, F.; Mele, A.; Caminiti, R.; Triolo, A., Mesoscopic Structural Organization in Triphilic Room Temperature Ionic Liquids. *Faraday Discuss.* **2013,** *167*, 499-513.

68. Triolo, A.; Russina, O.; Fazio, B.; Appetecchi, G. B.; Carewska, M.; Passerini, S., Nanoscale Organization in Piperidinium-Based Room Temperature Ionic Liquids. *J. Chem. Phys* **2009,** *130*, 164521.

69. Olga, R.; Alessandro, T.; Lorenzo, G.; Ruggero, C.; Dong, X.; Larry, G. H., Jr.; Richard, A. B.; Edward, L. Q.; Natalia, P.; Kenneth, R. S., Morphology and Intermolecular Dynamics of 1-Alkyl-3-Methylimidazolium Bis{(trifluoromethane)sulfonyl}amide Ionic Liquids: Structural and Dynamic Evidence of Nanoscale Segregation. *J. Condens. Matter Phys.* **2009,** *21*, 424121.

70. Canongia Lopes, J. N. A.; Pádua, A. A. H., Nanostructural Organization in Ionic Liquids. *J. Phys. Chem. B* **2006,** *110*, 3330-3335.

71. Canongia Lopes, J. N.; Costa Gomes, M. F.; Pádua, A. A. H., Nonpolar, Polar, and Associating Solutes in Ionic Liquids. *J. Phys. Chem. B* **2006,** *110*, 16816-16818.

72. Cook, A. G.; Wardell, J. L.; Imrie, C. T., Carbohydrate Liquid Crystals: Synthesis and Characterisation of the Methyl-6-O-(n-acyl)-α-d-glucopyranosides. *Chem. Phys. Lipids* **2011,** *164*, 118-124.

73. Cook, A. G.; Wardell, J. L.; Brooks, N. J.; Seddon, J. M.; Martínez-Felipe, A.; Imrie, C. T., Non-Symmetric Liquid Crystal Dimer Containing a Carbohydrate-Based mMoiety. *Carbohydr. Res.* **2012,** *360*, 78-83.

74. Ovejero, P.; Mayoral, M. J.; Cano, M.; Campo, J. A.; Heras, J. V.; Fernández-Tobar, P.; Valién, M.; Pinilla, E.; Torres, M. R., Mesomorphism of Four-Coordinated Four-Chained Metal

Complexes Based on Pyrazolylpyridine Derivatives. *Molecular Crystals and Liquid Crystals* **2008,** *481*, 34-55.

75. Marzec, M.; Mikułko, A.; Wróbel, S.; Hanczar, M.; Haase, W.; Dąbrowski, R., Influence of Molecular Structure on Phase Diagram and Ferroelectric Behaviour. *Ferroelectrics* **2006,** *343*, 181-191.

76. Li, X.; Bruce, D. W.; Jean'ne, M. S., Dicationic Imidazolium-Based Ionic Liquids and Ionic Liquid Crystals with Variously Positioned Fluoro Substituents. *Journal of Materials Chemistry* **2009,** *19*, 8232-8238.

77. Coles, H., First Ferrocene-Containing Low Molar Mass Organosiloxane Liquid-Crystalline Materials. *Journal of Materials Chemistry* **1999,** *9*, 1085-1090.

78. Chakraborty, L.; Chakraborty, N.; Choudhury, T. D.; Phani Kumar, B.; Mandal, A. B.; Rao, N. V., Synthesis, Mesomorphic and Photo-Physical Properties of Few *d*-and *f*-Block Metals Coordinated to Polar Schiff's Bases. *Liq. Cryst.* **2012,** *39*, 655-668.

79. Cowling, S. J., Optical Microscopy Studies of Liquid Crystals. In *Handbook of Liquid Crystals.* , J.W. Goodby, C. T., P. Raynes, H. Gleeson, T. Kato and P.J. Collings, Ed. Wiley-VCH Verlag GmbH & Co. KGaA.: Weinheim, 2014.

80. Jackson, G. P.; Duckworth, D. C., Electrospray Mass Spectrometry of Undiluted Ionic Liquids. *Chem. Commun.* **2004**, 522-523.

81. Liddel, U.; Ramsey, N. F., Temperature Dependent Magnetic Shielding in Ethyl Alcohol. *J. Chem. Phys* **1951,** *19*, 1608-1608.

82. Arnold, J. T.; Packard, M. E., Variations in Absolute Chemical Shift of Nuclear Induction Signals of Hydroxyl Groups of Methyl and Ethyl Alcohol. *J. Chem. Phys* **1951,** *19*, 1608-1609.

83. Muller, N.; Reiter, R. C., Temperature Dependence of Chemical Shifts of Protons in Hydrogen Bonds. *J. Chem. Phys* **1965,** *42*, 3265-3269.

84. Garcia-Viloca, M.; Gelabert, R.; González-Lafont, À.; Moreno, M.; Lluch, J. M., Temperature Dependence of Proton NMR Chemical Shift As a Criterion To Identify Low-Barrier Hydrogen Bonds. *J. Am. Chem. Soc.* **1998,** *120*, 10203-10209.

85. Sośnicki, J. G.; Hansen, P. E., Temperature Coefficient of NH Chemical Shifts of Thioamides and Amides in Relation to Structure. *J. Mol. Struct.* **2004,** *700*, 91-103.

86. Kontogianni, V. G.; Charisiadis, P.; Primikyri, A.; Pappas, C. G.; Exarchou, V.; Tzakos, A. G.; Gerothanassis, I. P., Hydrogen Bonding Probes of Phenol –OH Groups. *Organic & Biomolecular Chemistry* **2013,** *11*, 1013-1025.

87. Che, P.; Lu, F.; Nie, X.; Huang, Y.; Yang, Y.; Wang, F.; Xu, J., Hydrogen bond distinction and activation upon catalytic etherification of hydroxyl compounds. *Chem. Commun.* **2015,** *51*, 1077-1080.

88. Charisiadis, P.; Kontogianni, V.; Tsiafoulis, C.; Tzakos, A.; Siskos, M.; Gerothanassis, I., ^{1}H-NMR as a Structural and Analytical Tool of Intra- and Intermolecular Hydrogen Bonds of Phenol-Containing Natural Products and Model Compounds. *Molecules (Basel, Switzerland)* **2014,** *19*, 13643-13682.

89. Che, P.; Lu, F.; Nie, X.; Huang, Y.; Yang, Y.; Wang, F.; Xu, J., Hydrogen Bond Distinction and Activation upon Catalytic Etherification of Hydroxyl Compounds. *Chem. Commun.* **2015,** *51*, 1077-1080.

90. Qiao, B.; Krekeler, C.; Berger, R.; Delle Site, L.; Holm, C., Effect of Anions on Static Orientational Correlations, Hydrogen Bonds, and Dynamics in Ionic Liquids: A Simulational Study. *J. Phys. Chem. B* **2008,** *112*, 1743-1751.

91. Gehrke, S.; von Domaros, M.; Clark, R.; Hollóczki, O.; Brehm, M.; Welton, T.; Luzar, A.; Kirchner, B., Structure and Lifetimes in Ionic Liquids and Their Mixtures. *Faraday Discuss.* **2018,** *206*, 219-245.

92. Skarmoutsos, I.; Welton, T.; Hunt, P. A., The Importance of Timescale for Hydrogen Bonding in Imidazolium Chloride Ionic Liquids. *Phys. Chem. Chem. Phys.* **2014,** *16*, 3675-3685.

93. Goodby, J. W.; Watson, M. J.; Mackenzie, G.; Kelly, S. M.; Bachir, S.; Bault, P.; Gode, P.; Goethals, G.; Martin, P.; Ronco, G., et al., The Dependence of Mesomorphic Behaviour on the Extent of Hydrogen-Bonding in Sugar Derived Polyols. *Liq. Cryst.* **1998,** *25*, 139-147.

94. Bradley, J. P.; Velaga, S. P.; Antzutkin, O. N.; Brown, S. P., Probing Intermolecular Crystal Packing in γ-Indomethacin by High-Resolution ^{1}H Solid-State NMR Spectroscopy. *Cryst. Growth Des.* **2011,** *11*, 3463-3471.

95. Hong, M.; Gross, J. D.; Rienstra, C. M.; Griffin, R. G.; Kumashiro, K. K.; Schmidt-Rohr, K., Coupling Amplification in 2D MAS NMR and Its Application to Torsion Angle Determination in Peptides. *J. Magn. Reson* **1997,** *129*, 85-92.

96. Cobo, M. F.; Achilles, A.; Reichert, D.; deAzevedo, E. R.; Saalwächter, K., Recoupled Separated-Local-Field Experiments and Applications to Study Intermediate-Regime Molecular Motions. *J. Magn. Reson* **2012,** *221*, 85-96.

97. deAzevedo, E. R.; Saalwachter, K.; Pascui, O.; de Souza, A. A.; Bonagamba, T. J.; Reichert, D., Intermediate Motions as Studied by Solid-State Separated Local Field NMR Experiments. *J. Chem. Phys* **2008,** *128*, 104505.

98. Bradley, J. P.; Tripon, C.; Filip, C.; Brown, S. P., Determining Relative Proton–Proton Proximities from the Build-up of Two-Dimensional Correlation Peaks in ^{1}H Double-Quantum MAS NMR: Insight from Multi-Spin Density-Matrix Simulations. *Phys. Chem. Chem. Phys.* **2009,** *11*, 6941-6952.

99. Saalwächter, K.; Ziegler, P.; Spyckerelle, O.; Haidar, B.; Vidal, A.; Sommer, J.-U., ^{1}H Multiple-Quantum Nuclear Magnetic Resonance Investigations of Molecular Order Distributions in Poly(dimethylsiloxane) Networks: Evidence for a Linear Mixing Law in Bimodal Systems. *J. Chem. Phys* **2003,** *119*, 3468-3482.

100. Saalwächter, K., ^{1}H Multiple-Quantum Nuclear Magnetic Resonance Investigations of Molecular Order in Polymer Networks. II. Intensity Decay and Restricted Slow Dynamics. *J. Chem. Phys* **2004,** *120*, 454-464.

101. Zorin, V. E.; Brown, S. P.; Hodgkinson, P., Quantification of Homonuclear Dipolar Coupling Networks from Magic-Angle Spinning ^{1}H NMR. *Mol. Phys.* **2006,** *104*, 293-304.

102. Ren, J.; Eckert, H., DQ-DRENAR: A New NMR Technique to Measure Site-Resolved Magnetic Dipole-Dipole Interactions in Multispin-1/2 Systems: Theory and Validation on Crystalline Phosphates. *J. Chem. Phys* **2013,** *138*, 164201.

103. Saalwächter, K., Proton Multiple-Quantum NMR for the Study of Chain Dynamics and Structural Constraints in Polymeric Soft Materials. *Prog. Nucl. Magn. Reson. Spectrosc.* **2007,** *51*, 1-35.

104. Chassé, W.; Valentín, J. L.; Genesky, G. D.; Cohen, C.; Saalwächter, K., Precise Dipolar Coupling Constant Distribution Analysis in Proton Multiple-Quantum NMR of Elastomers. *J. Chem. Phys* **2011,** *134*, 044907.

105. Saalwächter, K.; Klüppel, M.; Luo, H.; Schneider, H., Chain Order in Filled SBR Elastomers: A Proton Multiple-Quantum NMR Study. *Appl. Magn. Reson.* **2004,** *27*, 401.

106. Löser, L.; Saalwächter, K.; Mendes Ferreira, T., Liquid–liquid phase coexistence in lipid membranes observed by natural abundance ^{1}H–^{13}C solid-state NMR. *Phys. Chem. Chem. Phys.* **2018,** *20*, 9751-9754.

107. Han, J. H.; Kim, J. S.; Park, J. K.; Lee, K. W.; Jin, J. I.; Choi, E. H.; Lee, C. E., Nuclear Magnetic Resonance Study of the Smectic-Cholesteric Phase Transition in a Dimesogenic Liquid Crystal. *Curr. Appl. Phys.* **2014,** *14*, 1356-1359.

108. Di Pietro, M. E.; Celebre, G.; De Luca, G.; Zimmermann, H.; Cinacchi, G., Smectic Order Parameters via Liquid Crystal NMR Spectroscopy: Application to a Partial Bilayer Smectic A Phase. *Eur. Phys. J. E.* **2012,** *35*, 112.

109. Figueirinhas, J. L.; Cruzi, C.; Ribeiro, A. C.; Tinh, N. H., NMR Study of Molecular Order in a Liquid Crystal with Smectic A_d and Reentrant Nematic Mesophases. A Comparative Study with Models for the S_{Ad} Phase. *Mol. Cryst. Liq. Cryst.* **1992,** *212*, 263-270.

110. Kharkov, B. B.; Chizhik, V. I.; Dvinskikh, S. V., Low rf Power High Resolution ^{1}H–^{13}C–^{14}N Separated Local Field Spectroscopy in Lyotropic Mesophases. *J. Magn. Reson* **2012,** *223*, 73-79.

111. Hong, M.; Schmidt-Rohr, K.; Nanz, D., Study of Phospholipid Structure by ^{1}H, ^{13}C, and ^{31}P Dipolar Couplings from Two-Dimensional NMR. *Biophys. J.* **1995,** *69*, 1939-1950.

112. Ferreira, T. M.; Medronho, B.; Martin, R. W.; Topgaard, D., Segmental Order Parameters in a Nonionic Surfactant Lamellar Phase Studied with ^{1}H–^{13}C Solid-State NMR. *Phys. Chem. Chem. Phys.* **2008,** *10*, 6033-6038.

113. Veber, M.; Jallabert, C.; Strzelecka, H.; Jullien, O.; Davidson, P., Non-Symmetrical Dithiolium Salts Mesomorphic Properties. *Liq. Cryst.* **1990,** *8*, 775-785.

114. Hong, M.; Schmidt-Rohr, K.; Pines, A., NMR Measurement of Signs and Magnitudes of C-H Dipolar Couplings in Lecithin. *J. Am. Chem. Soc.* **1995,** *117*, 3310-3311.

TOC Graphic

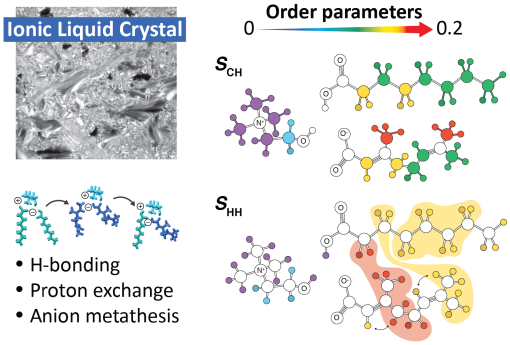
Ionic Liquid Crystal
Order parameters
0
0.2
S_{CH}
S_{HH}
• H-bonding
• Proton exchange
• Anion metathesis